Title page：

Manuscript title: GAS5 protects against osteoporosis by targeting UPF1/SMAD7 axis in osteoblast differentiation

Authors: Ming Li[1, 2*], Zhongyu Xie[1*], Jinteng Li[1, 2*], Jiajie Lin[1], Guan Zheng[1, 2], Wenjie Liu[1, 2], Su`an Tang[4], Shuizhong Cen[1, 2], Guiwen Ye[2], Zhaofeng Li[2], Wenhui Yu[1], Peng Wang[1#], Yanfeng Wu[3#], Huiyong Shen[1, 2#]

Affiliations:

[1]Department of Orthopedics, The Eighth Affiliated Hospital, Sun Yat-sen University, Shenzhen, 518033, People's Republic of China

[2]Department of Orthopedics, Sun Yat-sen Memorial Hospital, Sun Yat-sen University, Guangzhou, 510120, People's Republic of China

[3]Center for Biotherapy, Sun Yat-sen Memorial Hospital, Sun Yat-sen University, Guangzhou, 510120, People's Republic of China

[4]Department of Orthopedics, Zhujiang Hospital, Southern Medical University, Guangzhou, 510120, People's Republic of China

Email addresses:

Ming Li (542908648@qq.com) Zhongyu Xie (837802701@qq.com), Jinteng Li (869027295@qq.com), Jiajie Lin (linjj26@mail2.sysu.edu.cn), Guan Zheng (244700082@qq.com), Wenjie Liu (1510120964@qq.com), Su`an Tang (458448451@qq.com), Shuizhong Cen (793431985@qq.com), Guiwen Ye (345920339@qq.com), Zhaofeng Li (1002818922@qq.com), Wenhui Yu (649910237@qq.com), Peng Wang (wangpengsmh@foxmail.com), Yanfeng Wu (wuyf@mail.sysu.edu.cn), Huiyong Shen (shenhuiy@mail.sysu.edu.cn)

[*]These authors contributed equally.

[#]corresponding author

Huiyong Shen

Department of Orthopedics, The Eighth Affiliated Hospital, Sun Yat-sen University,

No. 3025, Shennan Middle Road, Futian District, Shenzhen, Guangdong, 518033,

China

Phone No: +86 139 2227 6368

Fax No: +86-0755-83012898

Email Address: shenhuiy@mail.sysu.edu.cn

Yanfeng Wu

Center for Biotherapy, Sun Yat-sen Memorial Hospital, Sun Yat-sen University

107 Yan Jiang Xi Road, Guangzhou 510120, China

Phone No: +86 136 0904 0860

Fax No: +86(0)20 81332612

Email Address: wuyf@mail.sysu.edu.cn

Peng Wang

Department of Orthopedics, The Eighth Affiliated Hospital, Sun Yat-sen University,

No. 3025, Shennan Middle Road, Futian District, Shenzhen, Guangdong, 518033,

China

Phone No: +86-0755-83012898

Fax No: +86-0755-83012898

Email Address: wangpengsmh@foxmail.com

Abstract

Osteoporosis is a common systemic skeletal disorder resulting in bone fragility and increased fracture risk. It is still necessary to explore its detailed mechanisms and identify novel targets for the treatment of osteoporosis. Previously, we found that a lncRNA named *GAS5* in human could negatively regulate the lipoblast/adipocyte differentiation. However, it is still unclear whether *GAS5* affects osteoblast differentiation and whether *GAS5* is associated with osteoporosis. Our current research found that *GAS5* was decreased in the bones and BMSCs, a major origin of osteoblast, of osteoporosis patients. Mechanistically, *GAS5* promotes the osteoblast differentiation by interacting with UPF1 to degrade *SMAD7* mRNA. Moreover, a decreased bone mass and impaired bone repair ability were observed in *Gas5* heterozygous mice, manifesting in osteoporosis. The systemic supplement of *Gas5*-overexpressing adenoviruses significantly ameliorated bone loss in an osteoporosis mouse model. In conclusion, *GAS5* promotes osteoblast differentiation by targeting the UPF1/SMAD7 axis and protects against osteoporosis.

Key word: osteoporosis, osteoblast differentiation, bone marrow stromal cells, *GAS5*

Introduction

Osteoporosis is a systemic skeletal disease that manifests as low bone mass and microarchitectural deterioration of bone tissue(***Yang, et al.,2019***). Individuals with osteoporosis are at a higher risk of fragility fractures(***Eastell, et al.,2016***). Over 200 million people worldwide suffer from this disease, and this number is gradually increasing(***Lizneva, et al.,2018***). Fractures caused by osteoporosis lead to functional disruption and pain along with an enormous therapeutic cost. In the United States and European Union, osteoporotic fractures have been estimated to cost $20 billion to $30 billion annually(***Lorentzon,2019***). Although many studies on osteoporosis have been conducted in recent years, more effective diagnostic and curative targets need to be explored for osteoporosis.

The imbalance between bone and fat mass is a typical feature of the osteoporosis pathogenesis(***de Paula and Rosen,2019***; ***de Paula and Rosen,2017***; ***Infante and Rodríguez,2018***). Recent studies have demonstrated that the abnormal differentiation capacities of bone marrow stromal cells (BMSCs) play an important role in this critical pathogenesis of osteoporosis(***Li, et al.,2019***; ***Ma, et al.,2018***). BMSCs are stem cells that possess self-renewal and multiple differentiation abilities(***Grayson, et al.,2015***). As the major origins of osteoblasts and adipocytes, BMSCs maintain their balance between osteoblast and adipocyte, which are regulated by various molecular checkpoints(***Anthony and Link,2014***; ***Williams and Hare,2011***). The abnormal expression of these molecules disrupts the osteoblast and adipocyte differentiation

balance and leads to disordered bone metabolism, ultimately resulting in disease development(***Xu, et al.,2018***; ***Zheng, et al.,2020***). Therefore, identifying these critical targets of osteoblast and adipocyte differentiation will be significantly helpful for the early diagnosis and treatment of diseases.

Long noncoding RNAs (lncRNAs) are a type of RNA longer than 200 nt and do not have protein-coding potential(***Marchese, et al.,2017***). The various and vital functions of lncRNAs in cell biology have been proven in numerous studies(***Tang, et al.,2017***; ***Yao, et al.,2019***). Previous studies have revealed that lncRNAs are involved in BMSCs osteoblast and adipocyte differentiation(***Xie, et al.,2019***). *GAS5* is a well-researched lncRNA that widely contributes to various cell biology functions such as immunity, tumor generation and metastasis(***Renganathan, et al.,2014***; ***Sun, et al.,2017***; ***Wang, et al.,2016***). In our previous study, we demonstrated that *GAS5* negatively affected the adipoytes differentiation through the *miR-18a*/CTGF pathway(***Li, et al.,2018***). Other researchers also recognized the crucial role of *GAS5* in BMSCs differentiation. For example, the researches of Wang, X etc. indicated that *Gas5* could promotes osteogenic differentiation of bone marrow mesenchymal stem cells by FOXO1 in mouse(***Wang, et al.,2019***). However, the effect of *GAS5* on human osteoblast differentiation and its role in osteoporosis have not been clearly clarified.

In our current research, we found that the level of *GAS5* was decreased in both the bones and BMSCs of osteoporosis patients. Molecular and in vivo studies revealed

that *GAS5* promoted the osteoblast differentiation through the UPF1/SMAD7 axis. Furthermore, *Gas5* heterozygous mice showed decreased bone mass and an impaired bone repair capacity as an osteoporotic phenotype. Bone loss was found to be alleviated in an osteoporosis mouse model after systemic application with *Gas5*-overexpressing adenoviruses. These findings consistently support the hypothesis that the lncRNA GAS5 acts as a protective target in osteoporosis by regulating osteoblast differentiation.

Results

GAS5 decreased in osteoporosis and positively correlated with the osteoblast differentiation

Eight osteoporosis patients who suffered from femoral neck fractures and 8 patients with hip dysplasia and 8 normal controls with car accident requiring surgery were recruited (Supplementary file 3). BGLAP and COL1A1 immunohistochemical staining confirmed the decrease in the bone formation marker in osteoporosis patients (Figure 1A). The mRNA level of *GAS5* in both bone tissues and BMSCs was decreased in patients with osteoporosis compared to in those with hip dysplasia and normal control (Figure 1B-C), which indicated that *GAS5* expression was closely related to bone metabolism in osteoporosis. Given the crucial role of BMSCs in osteoporosis, we explored the variation tendency of *GAS5* expression during osteoblast differentiation of BMSCs. The results showed that *GAS5* was upregulated

along with the induction of osteogenesis, as shown by ARS assays, ALP staining, ALP tests and qPCR (Figure 1D-E, Figure 1-figure supplement 1). In addition, there was a positive relationship between the expression of *GAS5* and the quantification of ARS staining (Figure 1F) or ALP activity (Figure 1-figure supplement 2A) or *RUNX2*/*COL1A11*/*BGLAP* mRNA expression (Figure 1-figure supplement 2B-D in osteoblast differentiation. The distribution of lncRNAs is crucial for their function in cell behavior. As shown in Figure 1G, the distribution of *GAS5* was more abundant in the cytoplasm. This tendency remained unchanged after induction (Figure 1H-I).

Figure 1 with 2 supplements

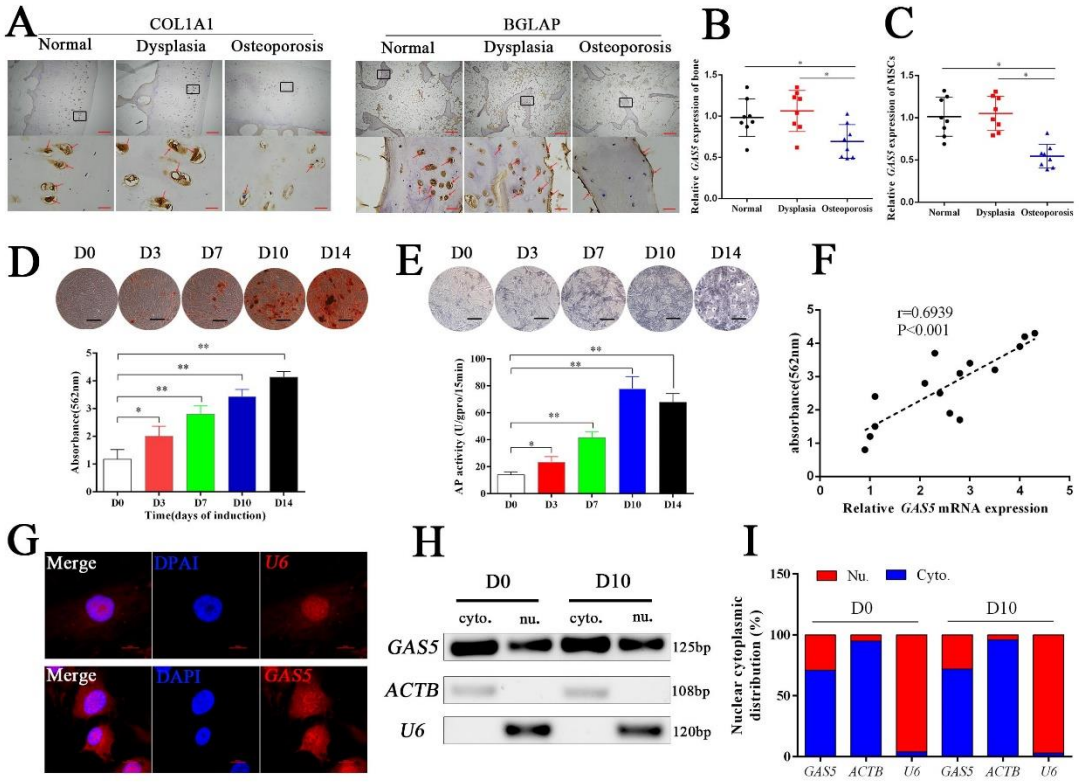

***GAS5* decreased in osteoporosis and positively correlated with the osteoblast differentiation.**

(A) COL1A1 and BGLAP immunohistochemical staining of the femur head from hip

dysplasia and osteoporosis patients. The red arrow shows typical staining. Scale bar, (upper, 500 μm; lower, 50 μm). (B) qRT-PCR analysis of *GAS5* isolated from cancellous bone between 8 patients with postmenopausal osteoporosis and 8 patients with hip dysplasia (n=8). (C) *GAS5* mRNA expression level in BMSCs isolated from hip dysplasia and osteoporosis patients (n=8). (D) ARS staining during the osteogenic differentiation of MSCs (top). Alizarin red staining quantification during the osteogenic differentiation of MSCs. (bottom) (n=15). (E) ALP staining and ALP assays in the osteoblast differentiation. (F) The relation of *GAS5* and Alizarin red staining quantification in the osteoblast differentiation (n=15). **G** *GAS5* RNA FISH in BMSCs. *U6* as the positive control. Scale bar, 50 μm. (H, I) Nuclear and cytoplasmic fractionation assay following agarose gel electrophoresis and analysis of *GAS5* in the osteoblast differentiation. ACTB (actin β) and U6 were used as the positive controls.

Figure 1-Figure supplement 1

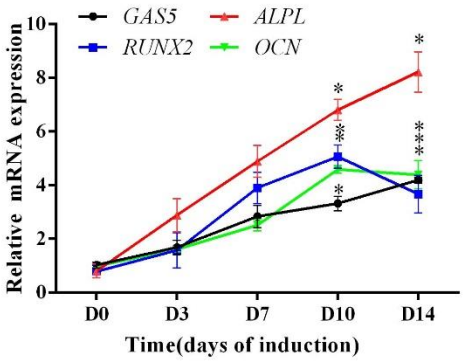

Gene marker expression of BMSCs osteoblast differentiation.

Relative mRNA expression of *GAS5*, *BGLAP*, *ALPL*, and *RUNX2* along with the day of human BMSCs osteogenic differentiation.

Figure 1-Figure supplement 2

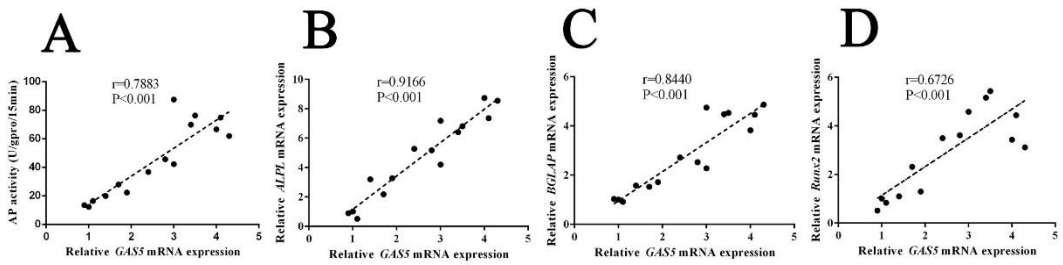

The relation of *GAS5* and the other makers of MSCs in the osteoblast differentiation

(A) The correlation of *GAS5* and ALP assay during osteogenic differentiation of MSCs (n=15). (B, C, D) The correlation of *GAS5* and *ALPL*, *BGLAP*, and *RUNX2* during osteogenic differentiation of MSCs (n=15).

Decreasing GAS5 inhibited the osteoblast differentiation in vitro and in vivo

To explore the function of *GAS5* in osteoblast differentiation, two siRNAs with better knockdown efficiency were chosen (Figure 2A) to construct the *GAS5*-knockdown lentiviruses (shRNA-1, shRNA-2). Decreased osteoblast differentiation was shown in the ARS assay (Figure 2B) and ALP assay (Figure 2C) after decreasing *GAS5* expression. The expression of osteogenesis markers, including *RUNX2*, *COL1A1*, *BGLAP*, *ALPL* and *SP7*, showed consistent results at both the mRNA (Figure 2D) and protein levels (Figure 2-figure supplement 1A-B). Then, we constructed a in vivo bone formation experiment to determine the role of *GAS5* in osteoblast differentiation. The new bone formation shown by H&E, Masson staining and BGLAP immunohistochemical staining in the shGAS5 group was significantly lower than that in the control group (Figure 2E, Figure 2-figure supplement 2).

Figure 2 with 2 supplements

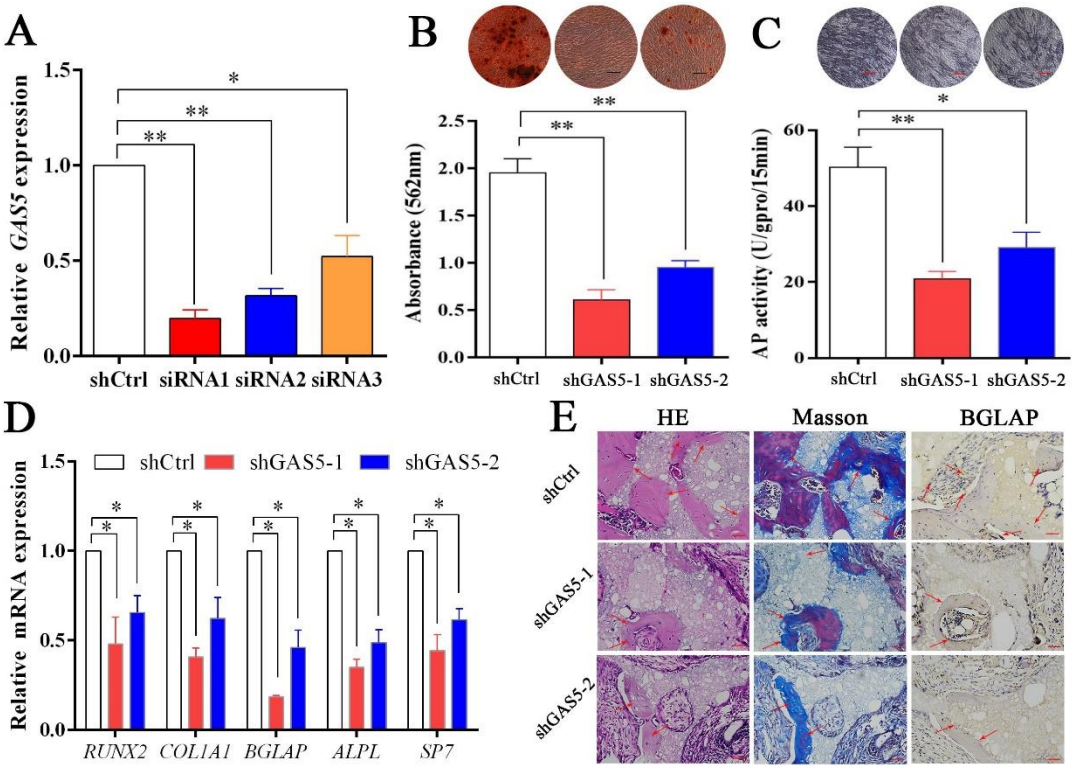

Decreasing *GAS5* inhibited the osteoblast differentiation in vitro and in vivo. (A) *GAS5* siRNA knockdown efficiency tested by qRT-PCR. (B) ARS staining and quantification in the *GAS5* knockdown or control group. Scale bar, 500 μm. (C) ALP staining and ALP tests in the *GAS5* knockdown or control group. Scale bar, 500 μm. (D) Relative *RUNX2*, *ALPL*, *BGLAP*, *COL1A1*, and *SP7* expression in the *GAS5* knockdown or control group. (E) H&E staining, Masson staining and *Bglap* immunohistochemical staining of HA/TCP in the *GAS5* knockdown or control group. The red arrow shows typical bone formation. Scale bar, 100 μm; n=5. Each cellular experimental group was repeated at least three times.

Figure 2-figure supplement 1

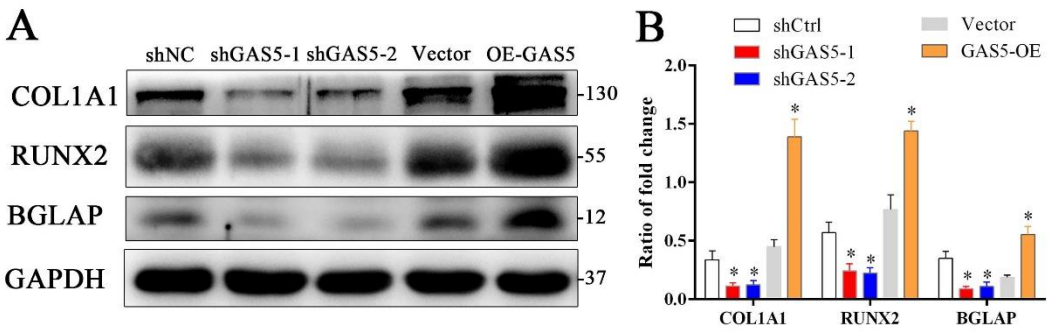

Western blot analysis and quantification of osteogenesis markers.

(A) Western blot analysis and quantification of osteogenesis markers (COL1A1, RUNX2, BGLAP) in *GAS5* knockdown or overexpression conditions. (B) Quantification of Western blot of osteogenesis markers (COL1A1, RUNX2, BGLAP) in GAS5 knockdown or overexpression conditions.

Figure 2-figure supplement 2

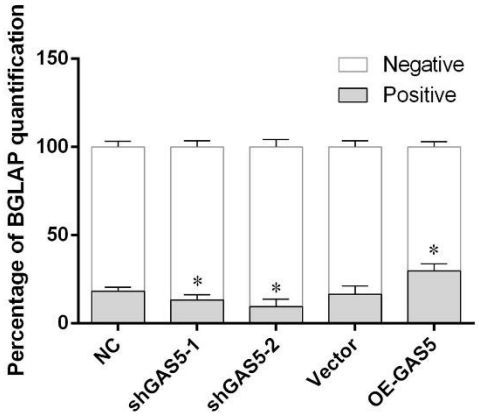

The quantification of BGLAP immunohistochemical staining.

The quantification of BGLAP immunohistochemical staining of in vivo bone formation tests in *GAS5* knockdown or overexpression treatment.

Increasing GAS5 promotes osteogenesis in vitro and in vivo

The expression level of *GAS5* in BMSCs was greatly increased in the OE-GAS5

(overexpression of GAS5) group (Figure 3A). After transfection with OE-GAS5, the osteoblast differentiation was significantly promoted, as determined by both ARS assays (Figure 3B) and ALP assays (Figure 3C). Similar results were confirmed by osteoblast marker expression at both the gene and protein levels (Figure 3D, Figure 3-figure supplement 1A-B). Moreover, increased bone formation in the OE-GAS5 group was observed in the bone formation model by H&E staining, Masson staining and BGLAP immunohistochemical staining (Figure 3E, Figure 3-figure supplement 2). These results indicated that *GAS5* positively promoted the osteoblast differentiation in vitro and in vivo.

Figure 3 with 2 supplements

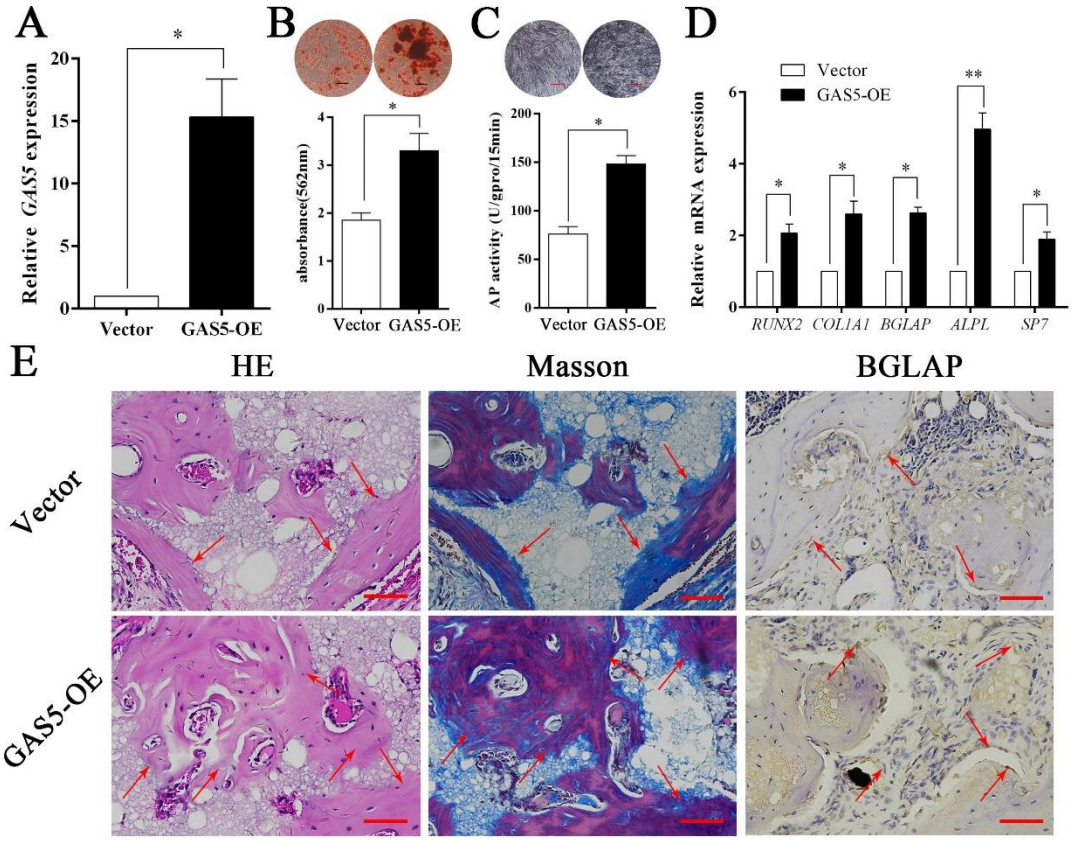

Increasing *GAS5* in BMSCs promotes osteoblast differentiation in vitro and in

vivo.

(A) Relative *GAS5* expression in the overexpression and control groups. (B) ARS staining and quantification in the *GAS5* overexpression or control group. Scale bar, 50 μm. (C) ALP staining and ALP tests in the *GAS5* overexpression or control group. (D) Relative *RUNX2*, *ALP*, *BGLAP*, *COL1A1*, and *SP7* expression in the *GAS5* overexpression or control group. (E) H&E, Masson staining and BGLAP immunohistochemical staining of HA/TCP in the *GAS5* overexpression or control group. The red arrow shows typical bone formation. Scale bar, 100 μm; n=5. Each cellular experimental group was repeated at least three times.

Figure 3-figure supplement 1

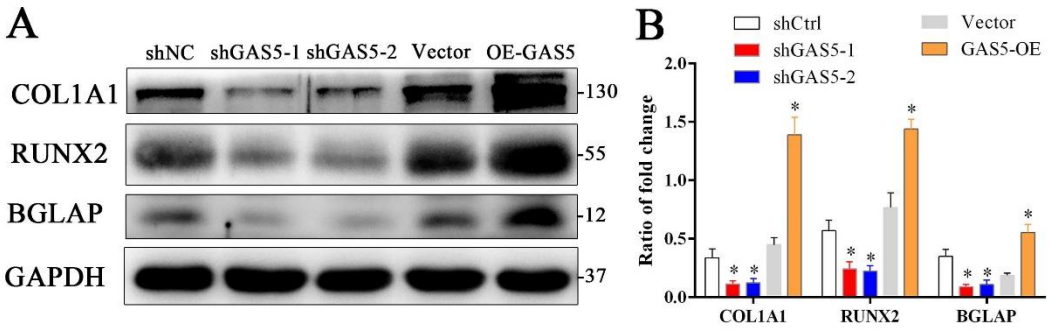

Western blot analysis and quantification of osteogenesis markers.

(A) Western blot analysis and quantification of osteogenesis markers (COL1A1, RUNX2, BGLAP) in *GAS5* knockdown or overexpression conditions. (B) Quantification of Western blot of osteogenesis markers (COL1A1, RUNX2, BGLAP) in *GAS5* knockdown or overexpression conditions.

Figure 3-figure supplement 2

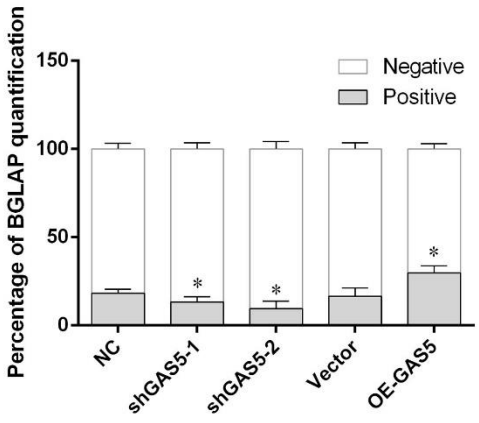

The quantification of BGLAP immunohistochemical staining.

The quantification of BGLAP immunohistochemical staining of in vivo bone formation tests in *GAS5* knockdown or overexpression treatment.

GAS5 functions by interacting with the UPF1 protein

To further investigate the detailed mechanism of *GAS5* in osteoblast differentiation, we first detected the adjacent genes of *GAS5* as in previous studies. The results showed that no significant changes in the adjacent genes were observed after inhibiting *GAS5* expression, indicating that it did not function through cis regulation (Figure 4-Figure Supplement 1). The lncRNA-protein interaction is also an important aspect of its function(***Marchese, et al.,2017***). Then, we performed an RNA pull-down assay to identify the interacting protein of *GAS5*. The mass spectrometry results indicated that UPF1, a DNA/RNA helicase at the crossroads of many critical cellular pathways for RNA and DNA maintenance(***Fiorini, et al.,2018***), was identified in the *GAS5* pull-down assay (Figure 4A). Western blot analysis of the *GAS5* pull-down protein confirmed that *GAS5* could interact with UPF1 specifically (Figure 4B), and a

RIP assay using the anti-UPF1 antibody further confirmed this conclusion (Figure 4C-D). In addition, the locations of *GAS5* and UPF1 in BMSCs partly overlapped, further indicating the interaction of *GAS5* and UPF1 (Figure 4E).

To further illuminate the specific interaction sites of the *GAS5*/UPF1 complex, we constructed *GAS5* mutant RNA according to the structure and sequence of *GAS5* (Figure 4F, Figure 4-Figure Supplement 2). RNA pull-down followed by Western blot analyses showed that *GAS5 (210-420)* was indispensable in the interaction with UPF1 and *GAS5* was unable to detect UPF1 when this sequence was lost (Figure 4G). UPF1 protein has been found to include three different functional regions, including CH, HD and SQ regions(***Dehecq, et al.,2018***; ***Fiorini, et al.,2018***). Based on the structure of UPF1, we constructed the Flag-tagged UPF1 truncation plasmid (Figure 4H), and RIP assays were performed to explore the *GAS5* interaction sites in UPF1. The results showed that UPF1-HD specifically combined with *GAS5* (Figure 4I-J), which indicated that UPF-HD is indispensable in the interaction of *GAS5* and UPF1.

Figure 4 with 2 supplements

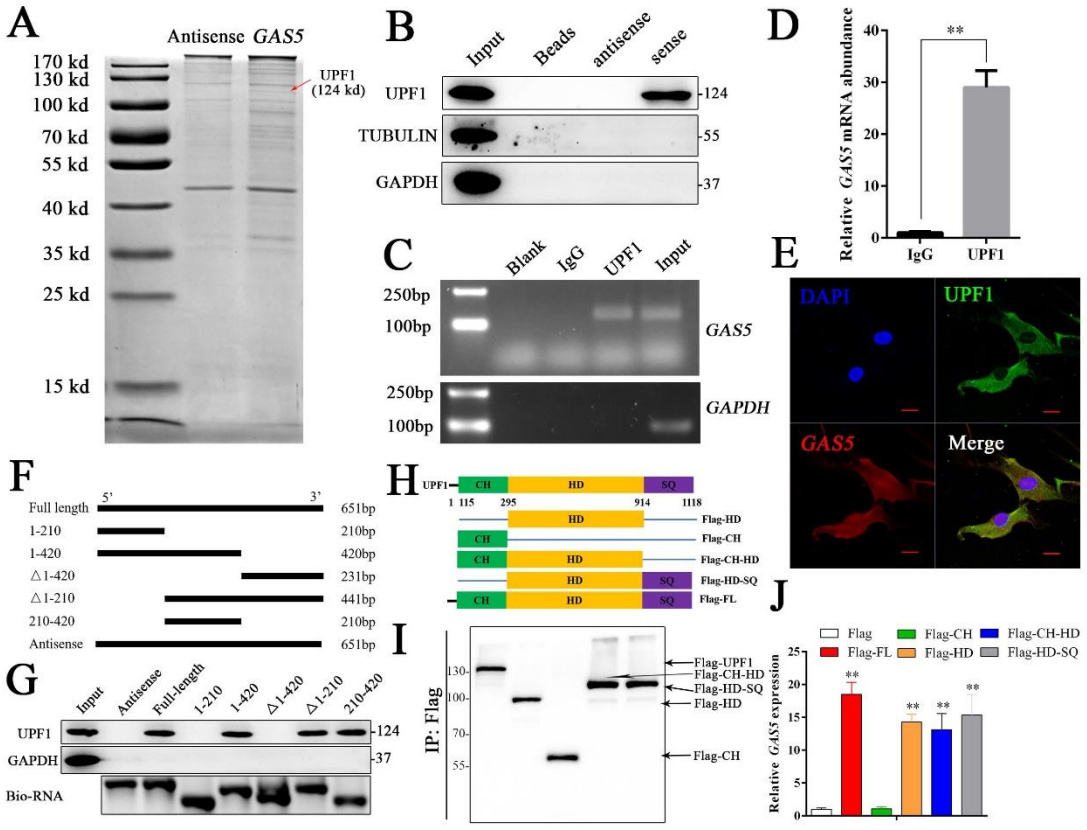

273

274 ***GAS5* functions by interacting with the *UPF1* protein.**

275 (A) Coomassie brilliant blue staining of RNA pull-down proteins in the *GAS5* sense
276 or antisense group. (B) The interaction between *GAS5* and UPF1 was confirmed by
277 Western blotting. (C, D) RIP assay analysis using the anti-UPF1 antibody revealed
278 that *GAS5* interacted with UPF1 in BMSCs, with GAPDH as a negative control. (E)
279 *GAS5* RNA FISH was performed in BMSCs and showed that *GAS5* could partly
280 colocalize with UPF1. Scale bar, 50 μm. (F) *GAS5* truncation sequence diagram. (G)
281 RNA pull-down assay with *GAS5* truncation sequences and analyzed by Western blot.
282 (H) UPF1 truncation diagram in a Flag tail. (I) Western blot analysis of the expression
283 efficiency of UPF1 truncations. (J) RIP assay used UPF1 truncations and was
284 analyzed by qRT-PCR. Each cellular experimental group was repeated at least three

times.

Figure 4-figure supplement 1

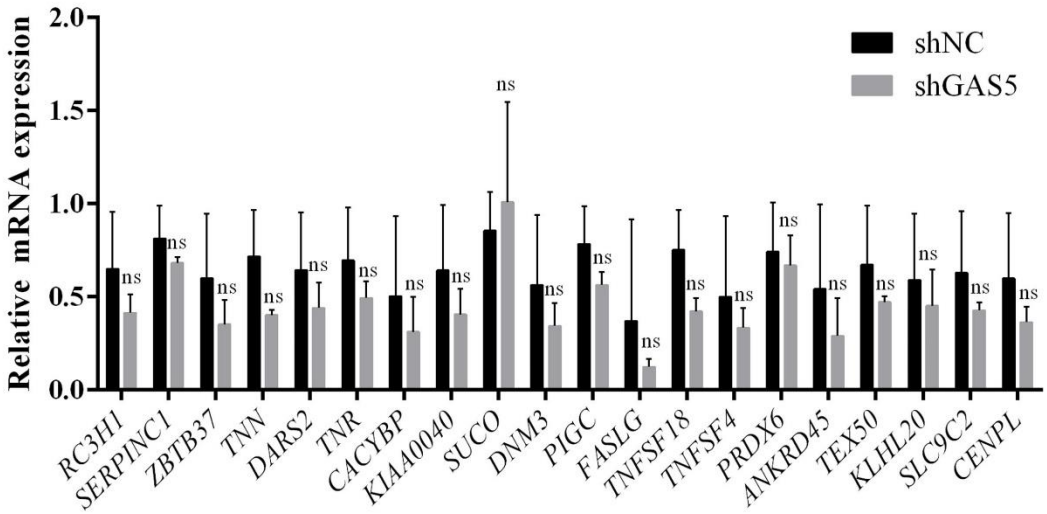

QRT-PCR analysis of the *GAS5* adjacent genes in *GAS5* knockdown conditions.

ZBTB37 (zinc finger and BTB domain containing 37), *RC3H1* (ring finger and CCCH-type domains 1), *SERPINC1* (serpin family C member 1), *ZBTB37* (zinc finger and BTB domain containing 37), *TNN* (tenascin N), *DARS2* (aspartyl-tRNA synthetase 2, mitochondrial), *TNR* (tenascin R), *CACYBP* (calcyclin binding protein), *KIAA0040* (KIAA0040), *SUCO* (SUN domain containing ossification factor), *DNM3* (dynamin 3), *PIGC* (phosphatidylinositol glycan anchor biosynthesis class C), *FASLG* (Fas ligand), *TNFSF18* (TNF superfamily member 18), *TNFSF4* (TNF superfamily member 4), *PRDX6* (peroxiredoxin 6), *ANKRD45* (ankyrin repeat domain 45), *TEX50* (testis expressed 50), *KLHL20* (kelch like family member 20), *SLC9C2* (solute carrier family 9 member C2 (putative)), *CENPL* (centromere protein L).

Figure 4-figure supplement 2

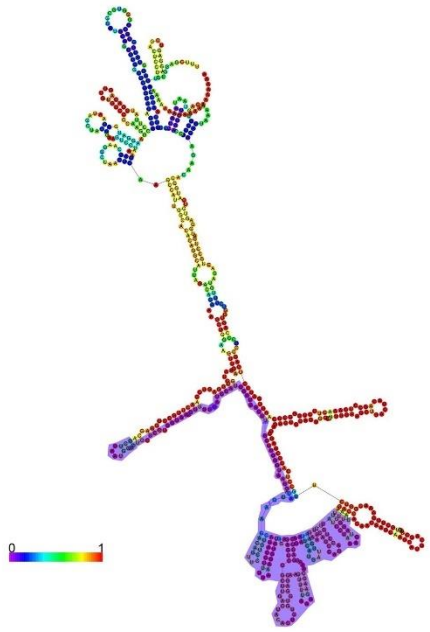

RNA fold model of *GAS5*.

The model was predicted on the *RNAfold web server* website (http://rna.tbi.univie.ac.at//cgi-bin/RNAWebSuite/RNAfold.cgi). The rainbow color means the base-pair probabilities of the predicted folded RNA. The area of *GAS5* combined with UPF1 was painted with lavender.

GAS5 interacts with UPF1 to accelerate SMAD7 decay

To further explore how *GAS5* interacted with UPF1 to regulate the osteoblast differentiation, the activation levels of three critical signaling pathways, including the TGF-β/SMAD1/5/8, catenin and ERK pathways, were analyzed. As shown in Figure 5A and Figure 5-figure supplement 1A-C, the SMAD1/5/8 signaling pathway was significantly decreased in the shGAS5 group but increased in the GAS5-OE group, and the catenin and ERK pathways were impervious to *GAS5* expression. Further

exploration of the TGF-β/SMAD1/5/8 pathway revealed that SMAD7, an inhibitor of SMAD1/5/8(***Miyazawa and Miyazono*,*2017***), was increased in the *GAS5* siRNA group and decreased in the *GAS5* overexpression group (Figure 5B and 5C). Other molecular factors in the SMAD1/5/8 pathways, such as BMP2, BMP4, BMP7 and SMAD6, were unchanged (Figure 5-figure supplement 2A-F). These results determined that SMAD7 in the SMAD1/5/8 signaling pathway was the target of the *GAS5*/UPF1 complex.

The RNA helicase UPF1 is one of the central molecules in nonsense-mediated mRNA decay (NMD) and Staufen-mediated mRNA decay(***M. Plank and Wilkinson*,*2018***). UPF1 knockdown could increase the expression of *SMAD7* as well as inhibit the activation of the SMAD1/5/8 pathway (Figure 5D-E). Based on the function of UPF1, a key molecule in mRNA nonsense-mediated decay, we hypothesized that *GAS5* could affect *SMAD7* mRNA stability by binding to UPF1 in BMSCs. First, we determined that UPF1 could bind to *SMAD7* mRNA by a RIP assay (Figure 5F). Next, we tested the mRNA abundance after the addition of actinomycin D, which is an inhibitor of DNA transcription, and found that the *SMAD7* mRNA decay speed was slower in the shGAS5 group but faster in the OE-GAS5 group at both the protein and RNA levels (Figure 5G-I). *UPF1* knockdown completely blocked the effect of *GAS5* on *SMAD7* mRNA decay speed (Figure 5J). Furthermore, the region of *GAS5 (210-420 bp)* could also enhance the speed of *SMAD7* mRNA decay and was blocked by UPF1 knockdown (Figure 5K). Knocking down UPF1 expression obviously blocked the function of *GAS5* in the regulation of osteoblast differentiation, as shown by ARS and

ALP assays (Figure 5L-M). These results indicated that *GAS5* positively regulated the osteoblast differentiation by interacting with UPF1 to accelerate *SMAD7* mRNA decay.

Figure 5 with 2 supplements

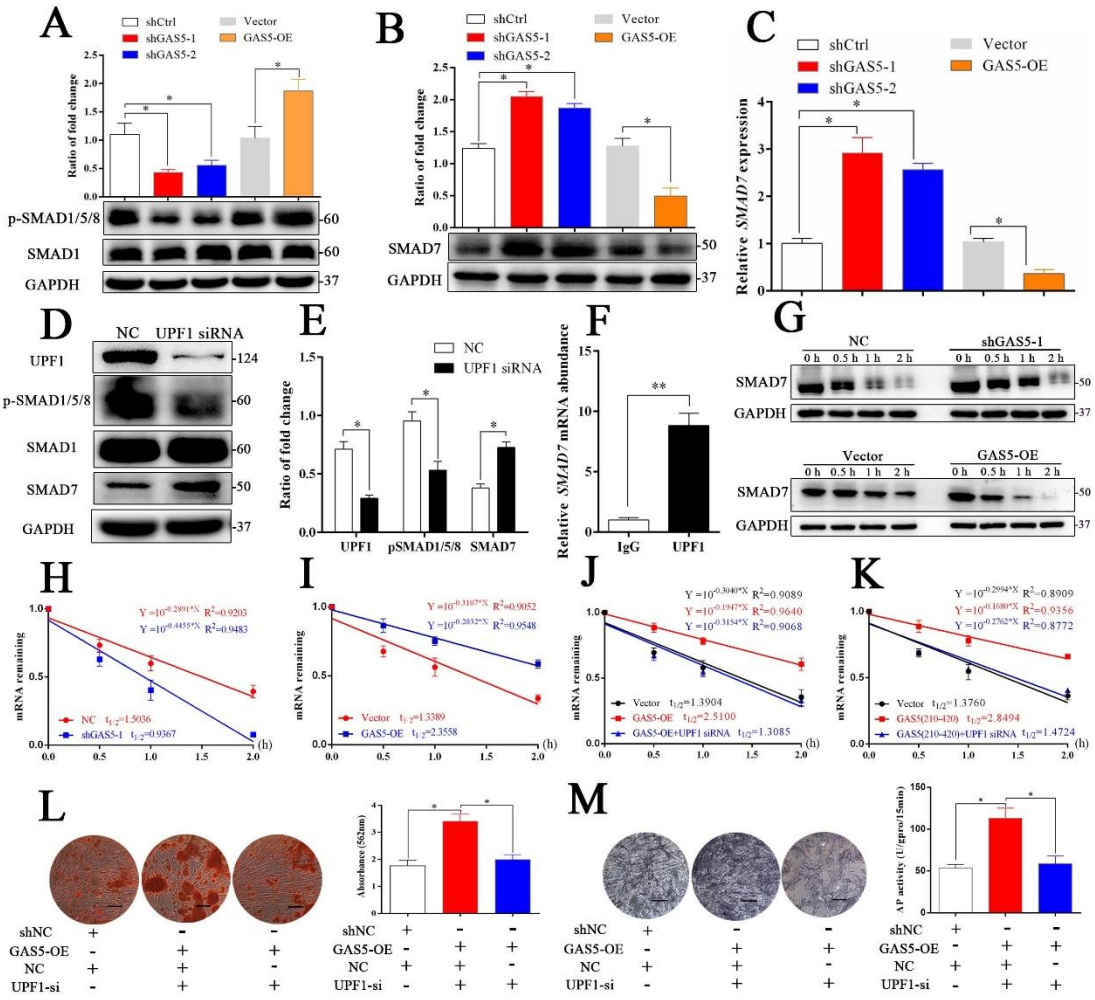

***GAS5* interacts with *UPF1* to accelerate *SMAD7* decay.**

(A) Western blot analysis of the activation pathway (pSMAD1/5/8, SMAD1) in *GAS5* knockdown or overexpression conditions. (B) SMAD7 was regulated by *GAS5* knockdown or overexpression by Western blot. (C) Relative *SMAD7* mRNA levels in *GAS5* knockdown or overexpression cells tested by qRT-PCR. (D, E) Western blot

346 analysis and quantification of pSMAD1/5/8/SMAD1 and SMAD7 in the UPF1
347 knockdown and control groups. (F) RIP assay with anti-UPF1 showed the binding of
348 UPF1 and *SMAD7* mRNA. (G) Western blot analysis in the *GAS5* knockdown,
349 overexpression and control groups after actinomycin D treatment. NC means the
350 negative control siRNA transfected group. It was also be treated by Actinomycin D
351 but as the control of *GAS5* shRNA-1. (H) Relative *SMAD7* mRNA expression in the
352 *GAS5* knockdown and control groups by actinomycin D treatment tested by qRT-PCR.
353 (I) Relative *SMAD7* mRNA expression in the *GAS5* overexpression and control
354 groups by actinomycin D treatment tested by qRT-PCR. (J, K) Relative *SMAD7*
355 mRNA expression by actinomycin D treatment under the condition of *UPF1* siRNA,
356 overexpression of a truncated form of *GAS5* or *GAS5* full-length. (L) ARS staining
357 and quantification in the *GAS5* overexpression and *UPF1* siRNA groups. Scale bar,
358 500 μm. (M) ALP staining and ALP tests in the *GAS5* overexpression and *UPF1*
359 siRNA groups. Scale bar, 500 μm. Each cellular experimental group was repeated at
360 least three times.

361 **Figure 5**-figure supplement 1

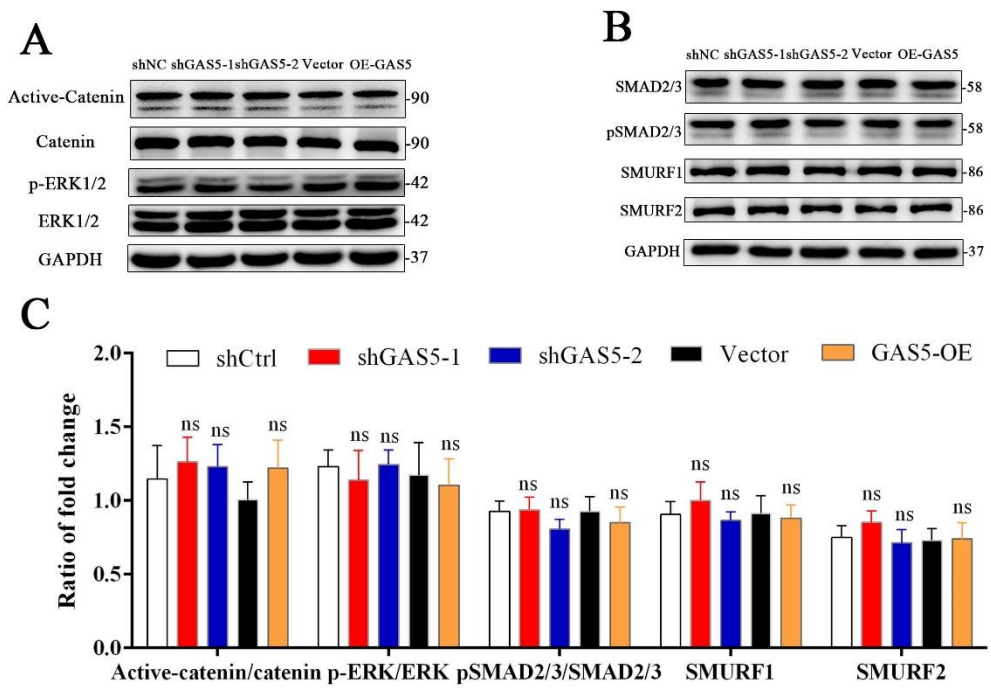

Western blot analysis of the pathway

(A, B) Western blot analysis and quantification of the pathway (catenin, ERK, SMAD2/3, SMURF1, SMURF2) in *GAS5* knockdown or overexpression conditions. (C) Quantification for Western blot analysis of β-catenin, ERK, SMAD2/3, SMURF1 and SMURF2.

Figure 5-figure supplement 2

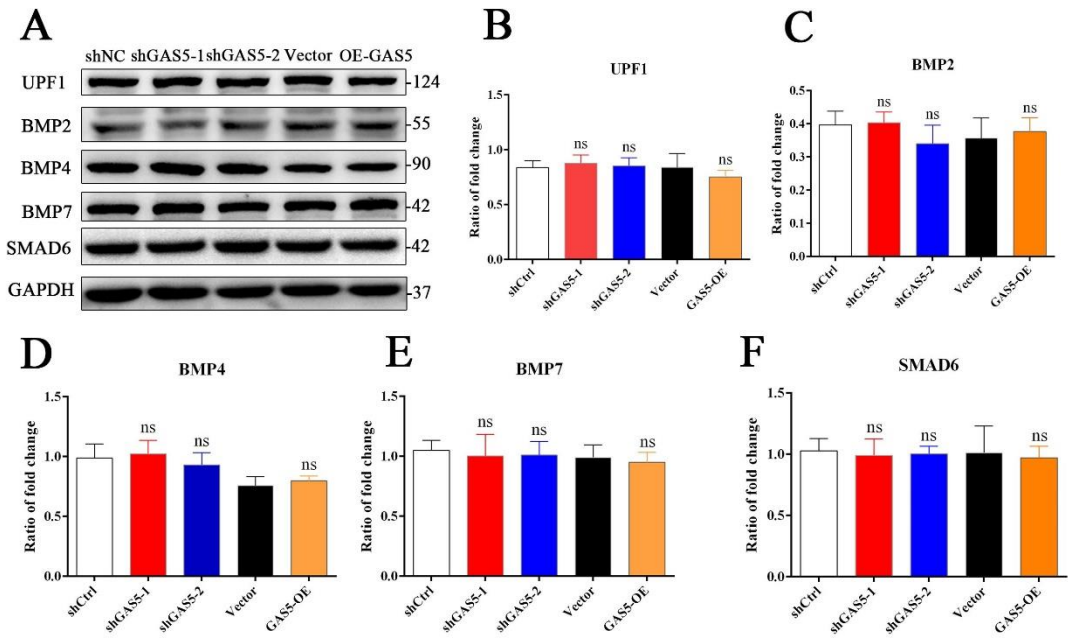

Western blot analysis of the molecular in BMP pathway

(A, B, C, D, E, F) Western blot analysis and quantification of BMP2, BMP4, BMP7, and SMAD6 in *GAS5* knockdown or overexpression conditions.

Gas5 heterozygous mice exhibit an osteoporotic phenotype and impaired bone repair capacity

To further explore the function of *GAS5* in bone metabolism, we constructed *Gas5* knockout mice. However, we used *Gas5* heterozygotes ($Gas5^{+/-}$) instead because all homozygous $Gas5^{-/-}$ mice unexpectedly died during the embryonic period. QRT-PCR analysis and DNA agarose gel electrophoresis proved that *Gas5* partly deletion was successful (Figure 6-figure supplement 1A-B). And *Gas5* in cancellous bone of $Gas5^{+/-}$mice decreased compared with the WT mice (Figure 6-figure supplement 1D). The heterozygous $Gas5^{+/-}$ mice survived normally and showed no changes in size, weight or appearance compared with their WT littermates ($Gas5^{+/+}$). However, the

384 *Gas5*$^{+/-}$ mice had less femoral cancellous bone than the WT mice, as shown by
385 micro-CT and its three-dimensional reconstruction results (Figure 6A). In addition,
386 H&E staining and *Bglap* immunohistochemical staining showed that bone trabeculae
387 were decreased in *Gas5*$^{+/-}$ mice (Figure 6B, Figure 6-figure supplement 2). In addition,
388 bone analysis from micro-CT showed that BV/TV, trabecular thickness, and
389 trabecular number were decreased, and BSA/BV and trabecular spacing were
390 increased in *Gas5*$^{+/-}$ mice compared with in WT mice (Figure 6C-G). As shown in
391 Figure 6H, decreased *Bglap* levels in the sera of the *Gas5*$^{+/-}$ group were observed
392 compared with those in the WT group. These results demonstrated that *Gas5*$^{+/-}$ mice
393 showed osteoporosis-like manifestations. The BMSC of *Gas5*$^{+/-}$ and WT group were
394 isolated and induced into osteoblast differentiation. The mRNA expression of *Gas5*,
395 *Upf1* and *Smad7* in BMSC of *Gas5*$^{+/-}$ and WT mice were detected. *Gas5* was
396 decreased in *Gas5*$^{+/-}$ mice while *Smad7* was increase compared with WT mice.
397 However, the level of *Upf1* mRNA has no significant change in two groups (Figure
398 6-figure supplement 1C). ARS and ALP staining showed that *Gas5*$^{+/-}$ mouse BMSCs
399 manifested a decreased osteoblast differentiation ability (Figure 6I-L). Furthermore,
400 the detection of proteins isolated from the tibia indicated that the Smad1/5/8 pathway,
401 rather than the catenin and ERK signaling pathways, was significantly lower in the
402 *Gas5*$^{+/-}$ group (Figure 6M-N, Figure 6-figure supplement 3). To determine the bone
403 repair ability, a skull defect model was constructed using *Gas5*$^{+/-}$ mice. Using
404 micro-CT, we found that the bone repair area on cranial bone was lower in *Gas5*$^{+/-}$
405 mice than in WT mice (Figure 6O-P). Collectively, these results suggest that *Gas5*$^{+/-}$

mice exhibit an osteoporotic phenotype and impaired bone repair capacity.

Figure 6 with 3 supplements

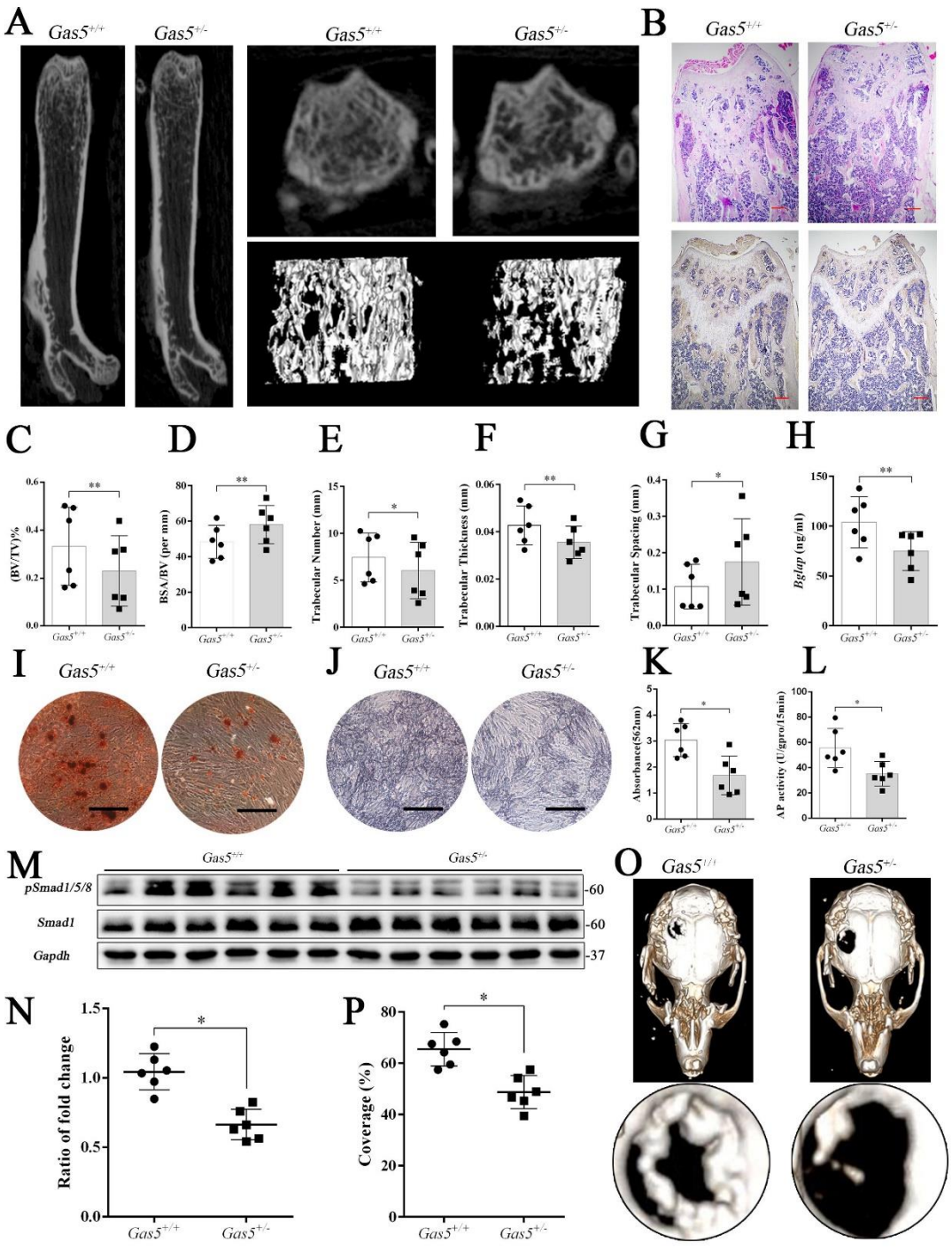

Gas5 **heterozygous mice exhibit an osteoporotic phenotype and impaired bone repair capacity.**

(A) Representative micro-CT analysis of the three-dimensional reconstruction graph for *Gas5*$^{+/-}$ (n=6) and WT mice (n=6). (B) Representative H&E staining (upper) and *Bglap* immunohistochemical staining (down) of the terminal femur of *Gas5*$^{+/-}$ (n=6) and WT mice (n=6). Scale bar, 500 μm. (C, D, E, F, G) BV/TV, BA/BV, trabecular thickness, trabecular number and trabecular spacing analysis of *Gas5*$^{+/-}$ (n=6) and WT mice (n=6). (H) Serum *Bglap* detection by ELISA in *Gas5*$^{+/-}$ (n=6) and WT mice (n=6). (I, K) ARS staining ARS and quantification of MSCs from *Gas5*$^{+/-}$ (n=6) and WT mice (n=6) Scale bar, 500 μm. (J) ALP staining of MSCs from *Gas5*$^{+/-}$ (n=6) and WT mice (n=6). (L) ALP tests of MSCs from *Gas5*$^{+/-}$ (n=6) and WT mice (n=6). Scale bar, 500 μm. (M, N) Western blot analysis for pSmad1/5/8/Smad1 in protein isolated from tibia of *Gas5*$^{+/-}$ (n=6) and WT mice (n=6). (O) Micro-CT three-dimensional images of cranial defects in *Gas5*$^{+/-}$ (n=6) and WT mice (n=6). (P) Bone recovery area analysis in *Gas5*$^{+/-}$ (n=6) and WT mice (n=6). Each cellular experimental group was repeated at least three times.

Figure 6-figure supplement 1

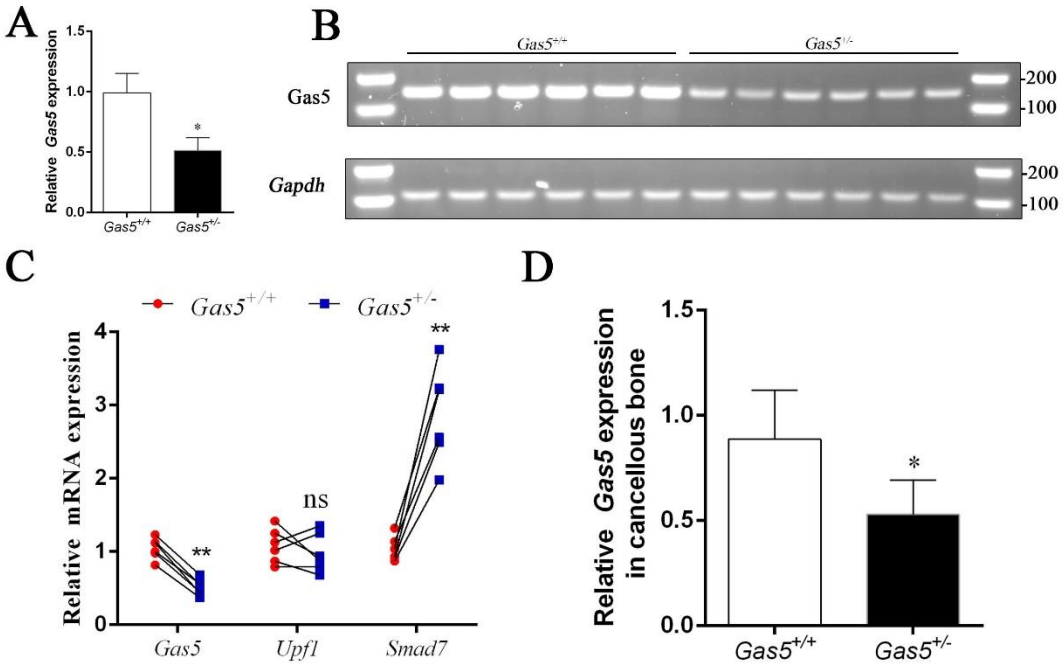

426

427 **Relative gene expression in mouse.**

428 (A, B) Relative *Gas5* expression in the tails of *Gas5*$^{+/+}$ (n=6) and *Gas5*$^{+/-}$ (n=6) mice

429 analyzed by qRT-PCR and agarose gel electrophoresis. (C) Relative mRNA

430 expression of *Gas5*, *Upf1* and *Smad7* in BMSC of *Gas5*$^{+/-}$ and WT mice (n=6). (D)

431 The mRNA level of *Gas5* in cancellous bone of *Gas5*$^{+/-}$mice and WT mice.

432 **Figure 6**-figure supplement 2

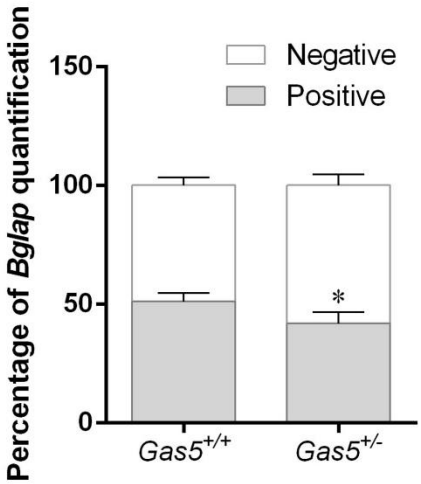

433

The quantification of *Bglap* immunohistochemical staining

The quantification of *Bglap* immunohistochemical staining of *Gas5*$^{+/-}$mice and WT mice.

Figure 6-figure supplement 3

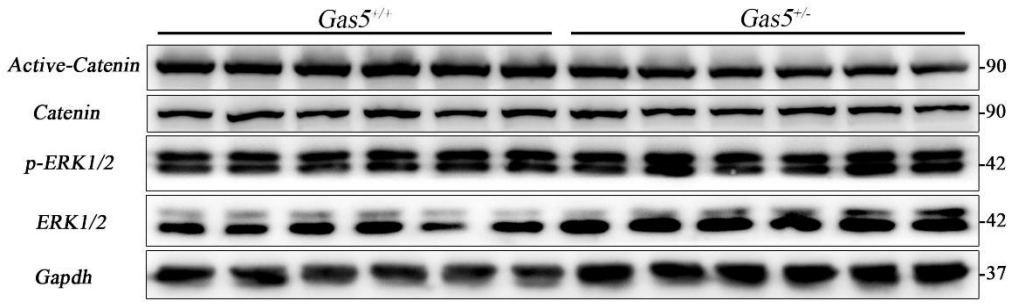

Western blot analysis of the pathway.

Western blot analysis of the pathway (β-catenin, ERK) in the protein from the tibia of *Gas5*$^{+/+}$ (n=6) and *Gas5*$^{+/-}$ mice (n=6).

Systemic transfection (tail vein injection) of Gas5-overexpressing adenoviruses alleviated bone loss in osteoporosis

To investigate the therapeutic effects of *Gas5* on osteoporosis, we induced osteoporosis in mice with dexamethasone (DXMS) and injected *Gas5*-overexpressing adenoviruses or negative control. After *Gas5*-overexpressing adenovirus injection, the bone mass was alleviated as determined by micro-CT (Figure 7A) as well as by H&E staining and *Bglap* immunohistochemical staining (Figure 7B, Figure 7-figure supplement 1). Bone analysis from micro-CT showed that the BV/TV, trabecular thickness and trabecular number were increasing in the *Gas5* adenovirus group

supplemented with drugs and had decreased BSA/BV and trabecular spacing compared with the negative control (Figure 7C-G). Taken together, these results suggest that *Gas5* may be a promising therapeutic target in osteoporosis.

Figure 7 with 1 supplement

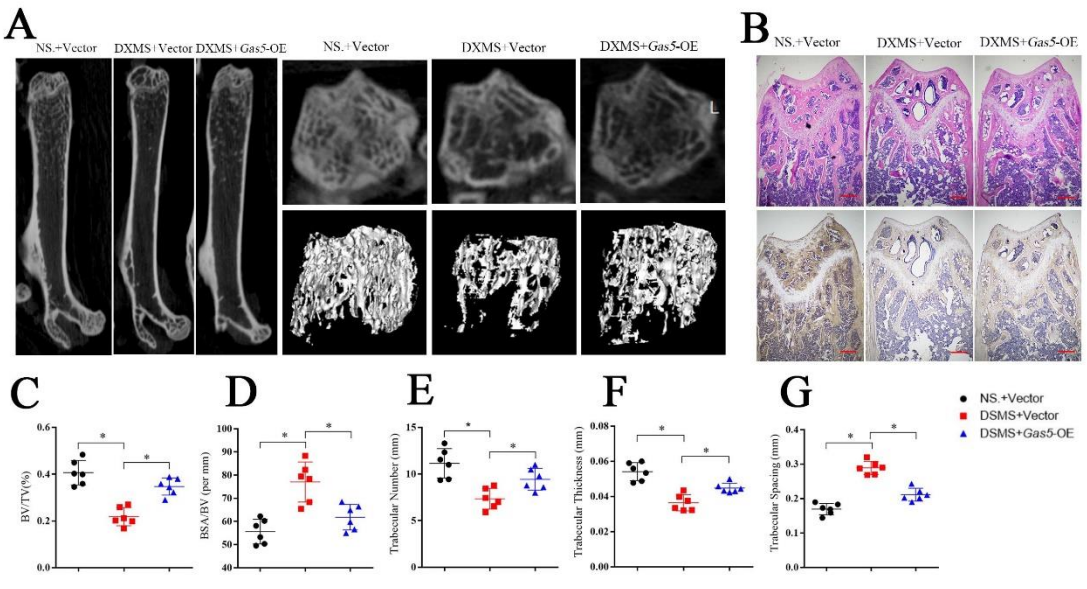

Systemic transfection (tail vein injection) of *Gas5*-overexpressing adenoviruses alleviated bone loss in osteoporosis.

(A) Micro-CT analysis of the control mice (n=6), osteoporosis mouse model (n=6) or *Gas5*-overexpressing adenovirus-treated mice (n=6). (B) H&E staining and *Bglap* immunohistochemical staining of the terminal femur of the control mice (n=6), osteoporosis mouse model (n=6) or *Gas5*-overexpressing adenovirus-treated mice (n=6). Scale bar, 500 μm. (C, D, E, F, G) BV/TV, BA/BV, trabecular thickness, trabecular number and trabecular spacing analysis for the control mice (n=6), osteoporosis mouse model (n=6) or *Gas5*-overexpressing adenovirus-treated group (n=6). DXMS: dexamethasone.

Figure 7-figure supplement 1

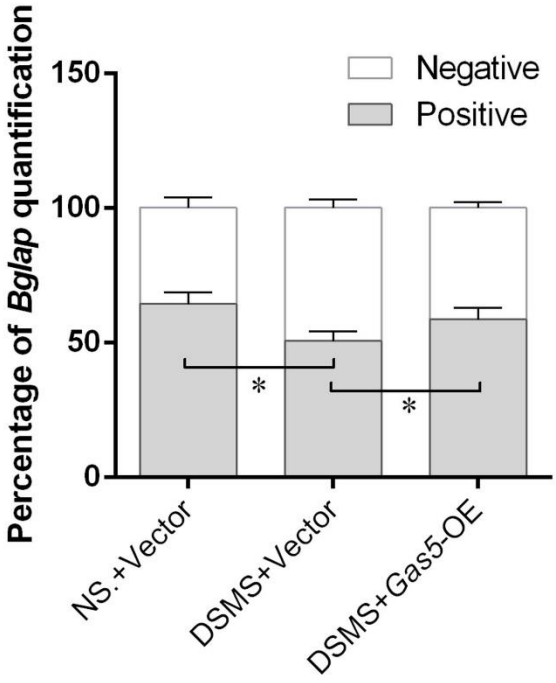

The quantification of *Bglap* immunohistochemical staining.

The quantification of *Bglap* immunohistochemical staining of the control mice (n=6), osteoporosis mouse model (n=6) or *Gas5*-overexpressing adenovirus-treated mice.

Discussion

Osteoporosis now needs more effective osteogenesis-promoting targets, as it currently has a limited therapeutic options(***Berry, et al.,2019***; ***Eastell, et al.,2016***). Therefore, exploration of the specific gene responsible for osteoporosis and identification of new therapeutic targets are especially important. Previously, we found that *GAS5* could negatively regulate the adipocyte differentiation(***Li, et al.,2018***). Herein, in our research, we found that as a protective target, *GAS5* decreases in both bone tissue and BMSCs, a major origin of osteoblast, of patients with osteoporosis. The osteoblast

differentiation could be positively regulated by *GAS5* both in vitro and in vivo. Mechanistically, *GAS5* could specifically interact with UPF1 to accelerate the decay of *SMAD7*, which in turn activates the SMAD1/5/8 signaling pathway. Furthermore, *Gas5* heterozygous mice showed decreased bone mass and an impaired bone repair capacity. Bone loss in the osteoporosis mouse model was improved by systemic transfection of *Gas5*-overexpressing adenoviruses. Considering all of these findings together, we concluded that *GAS5* is a critical molecule in the osteoblast and adipocyte differentiation and contributes to the pathogenesis of osteoporosis, emphasizing its novel role in the diagnosis and treatment of this disease.

As the major originating cells of osteoblasts and adipocytes, BMSCs antagonistically perform osteoblast or lipoblast differentiation both in vivo and in vitro(***Li, et al.,2018***). Physiologically, these differentiation abilities are balanced status and regulated by a variety of checkpoint molecules, including lncRNAs(***Grayson, et al.,2015***; ***Xie, et al.,2019***). However, the abnormal expression of these checkpoint molecules could disrupt the differentiation balance, leading to abnormal bone metabolism as well as disease development[8, 29, 30]. For example, the *lncRNA H19* could regulate osteogenesis by sponging *miR-675* and associating with cartilage regeneration, and abnormal *H19* expression was found in patients with osteoarthritis(***Huang, et al.,2015***; ***Liu, et al.,2017***). Previously, we found that *GAS5* inhibited the adipocyte differentiation through the *miR-18a*/CTGF axis(***Li, et al.,2018***). In our current research, we demonstrated that *GAS5* expression was positively correlated with the osteoblast

differentiation, as shown by ARS and ALP assays, as well as critical osteogenesis marker expression. Inhibiting or overexpressing *GAS5* accordingly decreased or increased the osteoblast differentiation both in vitro and in vivo. Collectively, these in vitro and in vivo results demonstrated that *GAS5* was another critical checkpoint molecule for the osteoblasts and adipocytes differentiation by promoting osteogenesis and inhibiting adipogenesis.

Recent research found that *GAS5* could regulate osteogenic differentiation in mouse mesenchymal stem cells(***Wang, et al.,2019***). While this result confirmed the role of *GAS5* in osteoblast differentiation, the physiological and pathological conditions as well as the molecular mechanisms are different between humans and mice. Therefore, it is important to further explore the detailed mechanisms of *GAS5* in the osteoblast differentiation of human. Critical signaling pathways for osteoblast differentiation, including SMAD1/5/8(***Grafe, et al.,2018***), catenin(***Kim, et al.,2015***) and ERK(***Ye, et al.,2018***), were detected, but only SMAD1/5/8 was regulated by *GAS5*. Furthermore, SMAD7, an inhibitory protein for the SMAD1/5/8 signaling pathway rather than for other molecules, was proven to be the target of *GAS5* in our study. Studies have found that SMAD7 inhibits the SMAD1/5/8 pathway and negatively regulates the osteoblast differentiation (***Li, et al.,2017***; ***Miyazawa and Miyazono,2017***). Surprisingly, we found that *GAS5* could not directly interact with SMAD7. Instead, *GAS5* showed a strong affinity for and interactions with UPF1, as shown by a series of results in our research.

UPF1 is a key molecule in mRNA nonsense-mediated decay (NMD)(***Dehecq, et al.,2018***). Recent studies indicated that UPF1 knockdown could inhibit the proliferation of colon cancer cells through the NMD mechanism(***Bokhari, et al.,2018***). Studies have confirmed that lncRNAs can combine with different functional proteins to exhibit various effects. For instance, lncRNAs can enhance protein recruitment toward the associated target(***Chen, et al.,2019***; ***Yari, et al.,2019***) or can strengthen/weaken the binding force of proteins and their targets(***Liu, et al.,2018***; ***Wang, et al.,2019***). In this research, we demonstrated for the first time the role of *GAS5* in RNA NMD of BMSCs via UPF1. By combining and collecting UPF1, *GAS5* accelerated the degradation of SMAD7 and therefore promoted osteoblast differentiation.

Further exploration in our studies indicated that *GAS5* binds to the HD domain of UPF1. The HD domain was the key functional area in UPF1-associated NMD. Mutations of the HD domain disrupt the RNA helicase activity of UPF1 and perturb the function of UPF1 in NMD(***Dehecq, et al.,2018***). Our results suggested that the binding of *GAS5* and UPF1 may strengthen the binding force of UPF1 and its target mRNA *SMAD7*. We speculated that in osteoblast differentiation, the increased expression of *GAS5* combined with UPF1 strengthened the binding of UPF1 and *SMAD7*, leading to the accelerated degradation of *SMAD7* and activation of the *SMAD1/5/8* pathway, ultimately promoting osteoblast differentiation.

Decreased bone mass and increased fat formation in bone are the main histopathological manifestations of osteoporosis(***Compston, et al.,2019***; ***Eastell, et al.,2016***; ***Infante and Rodríguez,2018***), which indicates an imbalance between the osteoblast and adipocyte differentiation in osteoporosis patients. Many studies have confirmed that BMSCs in osteoporosis patients possess a decreased osteogenic ability but an enhanced adipogenic ability(***de Paula and Rosen,2019***; ***Pagnotti, et al.,2019***), which is an important reason for the abnormal bone mass decrease and fat accumulation in bone marrow of osteoporosis patients. However, whether *GAS5* participated in these processes was not clearly clarified. In our research, we found that the level of *GAS5* expression was decreased in the bone tissue and BMSCs of osteoporosis patients, indicating that *GAS5* may be related to the progression of osteoporosis. To confirm this hypothesis, we constructed a global *Gas5* knockout mouse model to explore the role of *GAS5* in osteoporosis. However, global *Gas5* knockout caused unexpected lethality in the embryonic period, which indicated that *Gas5* was indispensable in the development of the embryo. Interestingly, the osteoporotic phenotype, including lower bone mass, was macroscopically and microscopically observed in surviving *Gas5* heterozygous mice, as shown by both micro-CT and histological staining, compared with in WT mice. Combining the above results, we speculated that decreased *Gas5* levels may change heterozygote bone mass by regulating the osteoblast differentiation. To further confirm the abnormal osteogenic ability of *Gas5* heterozygous mice, we constructed a cranial defect model and found that its bone repair ability was significantly weakened, which further

confirmed the dysfunction of osteoblast differentiation in *Gas5* heterozygous mice. However, the mechanism of cranial bone formation may not be analogous to what is observed for bone formation and or bone healing in the long bone (***Katsimbri*,*2017***; ***Catala, et al.*,*2019***). We do not know exactly how *Gas5* would impact long bone healing and that this is a needed future direction.

Currently, the treatment of osteoporosis is currently mainly aimed at osteoclasts(***Ensrud and Crandall*,*2017***; ***Roux and Briot*,*2018***), and the new therapy with *teriparatide* has shown a more curative effect in osteoporosis(***Minisola, et al.*,*2019***), which suggests that treatment options directed at osteoblasts are of great significance. Adenoviruses containing lncRNAs were used to treat mice and showed a significant therapeutic effect in many diseases, including ischemic myocardial injury(***Cai, et al.*,*2019***) and cardiac regeneration(***Ponnusamy, et al.*,*2019***). To clarify the possible role of *Gas5* in osteoporosis treatment, we supplemented *Gas5*-overexpressing adenoviruses in an osteoporosis mouse model based on the preceding results. Micro-CT, H&E staining and *Bglap* immunohistochemical staining showed that the bone loss in the *Gas5* overexpression group was more alleviated than the bone loss in the control group. These results indicate that *Gas5* not only participates in the pathogenesis of osteoporosis but also may be a promising therapeutic target.

In conclusion, we found that *GAS5* acts as a protective target in osteoporosis. The

protective function of *GAS5* was exhibited by promoting the osteoblast differentiation by the UPF1/SMAD7 axis. Targeting *GAS5* may greatly contribute to both the diagnosis and treatment of osteoporosis. However, several limitations still exist in our study. For example, more convincing evidence should be obtained by conducting experiments with an osteoblast-specific *Gas5* conditional knockout mouse. Further studies should be performed to address these issues in the future.

Materials and Methods

Animals

The use plan of all involving animals (including the type and number of mice, the specific operation plan, and the principle of optimal substitution, etc.) was proposed, and the final plan was determined after internal discussion in the research group. The animal plan finally approved by the Animal Use and Care Committee of the Eighth Affiliated Hospital of Sun Yat-sen University. *Gas5*$^{+/+}$ and *Gas5*$^{+/-}$ mice (B6/JNju-Gas5em1Cd1152/Nju, pure C57BL/6J background) were purchased from GemPharmatech Co., Ltd. (Nanjing, China). Male and female *Gas5*$^{+/+}$ and *Gas5*$^{+/-}$ mice were euthanized at 3 and 6 months of age.

Cell isolation and culture

Human BMSCs from 15 volunteers were isolated from bone marrow after informed consent was obtained in Center for Biotherapy, Sun Yat-sen Memorial Hospital. Briefly, bone marrow was extracted from the posterior superior iliac spine under

sterile conditions. BMSCs were purified, isolated and cultured using our previously reported methods. BMSCs at passage 2 were used in the experiments. BMSC identity was confirmed by the immunophenotype profile. The cells used in experiments were positive for the BMSC surface antigens CD29-phycoerythrin (PE), CD34-allophycocyanin (APC), and CD44-fluorescein isothiocyanate (FITC) and negative for CD45-FITC, CD105-FITC, and HLA-DR-PE. The source of BMSCs for *GAS5* location, function and mechanism exploration in BMSCs differentiation were from these 15 volunteers. Human tissue was obtained from healthy donors after informed consent was obtained. The MSCs of normal control, hip dysplasia and osteoporosis patients was isolated in the above method. The study was approved by the ethics committee of the Eighth Affiliated Hospital of Sun Yat-sen University (Shenzhen, People's Republic of China). After explaining in detail for the possible risks and importance of the research, as well as informing methods of privacy protection, we obtained the informed consent and consent publish signatures of all patients or normal donors.

Osteoblast differentiation and identification

For osteoblast differentiation, BMSCs were cultured in osteoblast differentiation medium (DMEM containing 10% FBS, 0.1 μM dexamethasone, 10 mM β-glycerol phosphate, 50 μM ascorbic acid, 100 IU/ml penicillin, and 100 IU/ml streptomycin) for 0–14 days. The medium was replaced every 3 days. The osteoblast differentiation was identified by alizarin red S (ARS) and alkaline phosphatase (ALP) assays as

follows.

ALP staining was performed according to the manufacturer's instructions on day 10. Briefly, the cells were washed with PBS 3 times for 5 minutes, and an appropriate amount of BCIP/NBT staining liquid was added. The samples were incubated at room temperature in the dark for 20 minutes until the color developed. The working fluid was removed, and the cells were washed with distilled water twice to stop the reaction, and pictures were taken under the microscope.

ARS staining was performed as described in our previous study. The cells were fixed with paraformaldehyde for 30 minutes and washed with PBS 3 times. Alizarin red staining solution was added, and the cells were stained for 15 minutes at room temperature. The cells were washed again with PBS 3 times, and photos were taken under the microscope. The cells were destained for 1 h at room temperature using 10% cetylpyridinium chloride monohydrate for ARS quantification. Afterwards, 200 μL of the liquid was transferred to a 96-well plate, and the spectrophotometric absorbance was measured at 562 nm.

RNA isolation, reverse transcription and qRT-PCR analyses

Total RNA was isolated from BMSCs with an RNA-Quick Purification Kit (ESscience, Guangzhou) and transcribed into complementary DNAs using a PrimeScript RT Reagent Kit (TaKaRa, Dalian) according to the manufacturer's instructions. Real-time PCR was performed using SYBR Green Premix Ex Taq (TaKaRa, Dalian). The data were standardized based on *GAPDH* expression, and the

657 $2^{-\Delta\Delta Ct}$ method was used to analyze the data and determine the relative expression of
658 each gene. The forward and reverse primers for each gene are listed in Supplementary
659 Table 1.
660
661 **Western blot and antibodies**
662 Cells and tissues were lysed in RIPA lysis buffer containing a protease inhibitor
663 cocktail. Protein lysates were separated by SDS polyacrylamide gel electrophoresis
664 (SDS-PAGE) and transferred onto PVDF membranes. Then, the membranes were
665 blocked with BSA and incubated with primary antibodies against UPF1 (1:5000,
666 ab109363, Abcam), SMAD7 (1:2000, MAB2029, RD system), SMAD1/5/9 (1:1000,
667 13820S, Cell Signaling Technology), SMAD1 (1:1000, 6944S, CST), beta-Catenin
668 (1:1000, 8480S, CST), Nonphospho (Active) β-Catenin (1:1000, 19807S, CST),
669 Phospho-p44/42 MAPK (Erk1/2) (1:1000, 4370, CST), p44/42 MAPK (Erk1/2)
670 (1:1000, 4695, CST), BMP2 (1:1000, ab14933, Abcam), BMP4 (1:1000,
671 ab124715-40 µl, Abcam), BMP6 (1:1000, ab155963-40 µl, Abcam), BMP7 (1:1000,
672 ab129156-40 µl, Abcam), SMAD6 (1:1000, ab80049, Abcam), GAPDH (1:5000,
673 AF0006, Beyotime), overnight at 4 °C. The protein signals were detected using
674 chemiluminescent reagents (Millipore) according to the manufacturer's instructions.
675
676 **Nuclear and cytoplasmic fractionation and agarose gel electrophoresis**
677 Cytoplasmic and nuclear RNA was extracted as described previously according to the
678 manufacturer's instructions (PARIS, Part Number AM1921). Cells were lysed in lysis

679 solution and isolated in cell disruption and cell fractionation buffer. qRT-PCR was
680 performed to analyze the RNA extracted from each of the fractions. The data were
681 analyzed to determine the nuclear and cytoplasmic levels of each RNA.
682 PCR products were collected with DNA loading buffer and separated on 1.2% agarose
683 containing 0.01% Gel Red (Biotium). Thereafter, DNA products were detected by UV
684 light and photographed for observation.
685
686 **RNA pull-down assay and mass spectrometry**
687 *GAS5* and its mutants were cloned into the pcDNA3.1(+) vector. Linearized
688 pcDNA3.1(+) expressing *GAS5*- or *GAS5*-deletion sequences was used as a template
689 to synthesize biotinylated *GAS5*, *GAS5* antisense or mutant sequences by the
690 TranscriptAid T7 High-Yield Transcription Kit (Thermo Fisher Scientific). A Pierce
691 RNA 3′ End Desthiobiotinylation Kit was used to attach a single desthiobiotinylated
692 cytidine bisphosphate to the 3′ end of the RNA strand. After biotin labeling, the
693 Pierce™ Magnetic RNA-Protein Pull-Down Kit (Thermo Fisher Scientific) was used
694 for the RNA pull-down assay following the manufacturer's suggestions. Labeled RNA
695 was captured using 50 μL of streptavidin magnetic beads in RNA Capture Buffer for
696 30 minutes at room temperature. RNA pull-down specificity was assessed by Western
697 blotting. The RNA-binding proteins were sequenced and identified by LC-MS as
698 described by BBI Life Sciences Corporation.
699
700 **RNA immunoprecipitation (RIP)**

RIP was performed using a previously described method(***Li, et al.,2018***). In brief, 5×10^6 cells were harvested by RIP lysis buffer and then incubated with RIP buffer containing magnetic beads conjugated to anti-UPF1 and anti-Flag antibodies. Purified rabbit IgG was used as a negative control. A positive control anti-SNRNP70 antibody was used for the RIP procedure. Then, immunoprecipitated RNAs were isolated and purified for quantitative PCR analysis to detect the presence of the target lncRNA.

Plasmid, lentivirus construction and infection

Three *GAS5* and *UPF1* siRNAs were designed and synthesized by GenePharma (Shanghai, China). Details of the sequences are shown in Supplementary Table 2. The best knockdown efficiency siRNA was selected to build the short hairpin RNA (shRNA) and construct the lentivirus by OBiO Technology (Shanghai) Corp., Ltd. *GAS5* lentiviruses, *Gas5*-overexpressing adenoviruses and the plasmids UPF1-Flag, CH-Flag, HD-Flag, CH-HD-Flag, and HD-SQ-Flag were constructed and purchased from OBiO Technology (Shanghai). Completed lentiviruses and adenoviruses were used to transfect BMSCs and animals, respectively, for functional testing. BMSCs were incubated with the lentiviruses for 24 h at a multiplicity of infection of 50.

Bone formation of BMSCs in vivo

BMSCs were transfected with lentiviruses (shGAS5-1, shGAS5-2, negative control, GAS5-OE or the vector) were cultured in osteoblast medium for 7 days prior to the in vivo study. The cells (5×10^5) were resuspended and planted onto 40 mg

hydroxyapatite/tricalcium phosphate (HA/TCP) scaffold. Then, the scafflods were implanted subcutaneously into the backs of 8-week-old BALB/c homozygous nude (nu/nu) mice. The implants were removed after 8 weeks and fixed in 4% paraformaldehyde. H&E, Masson and immunofluorescence staining were performed to analyze the new bone formation.

Collection of human bone samples

The femoral head was acquired during the surgery after signing informed consent with all donors. Eight postmenopausal osteoporosis patients with femoral neck fractures and 8 hip dysplasia patients requiring surgery and 8 normal control patients with the accident required surgery were recruited in this research. The characteristics of the study subjects are presented in Supplementary Table 3.

Fluorescent in situ hybridization (FISH)

For RNA FISH, a Ribo^{TM} Fluorescent In Situ Hybridization Kit (RiboBio company) was used to detect the RNA in BMSCs according to the manufacturer's instructions. In brief, cells in wells were fixed with 4% polyoxymethylene for 20 minutes, permeabilized and prehybridized in hybridization buffer and then hybridized at 55 °C for 1 h with a *GAS5* probe mix (RiboBio company). Stained samples were mounted with Fluoromount-G for confocal imaging. Images were obtained using an LSM 5 Exciter confocal imaging system (Carl Zeiss).

Osteoporosis mouse model construction and treatment

Glucocorticoid-induced C57BL/6J mice were used to establish an osteoporosis model (dexamethasone (DXMS) dosage: 2 mg/kg, hind leg muscle injection, 3 times a week for 8 weeks). A total of 5×10^{11} *Gas5*-overexpressing adenoviruses or control adenoviruses was injected into the mice from the tail vein. Eight weeks later, the serum and femur of the mice were acquired for micro-CT and staining studies.

Cranial defect experiment

Ten-week-old mice were anesthetized, and the skin was prepared, and the surgical area was strictly disinfected. The skin was incised with a scalpel, and the subcutaneous tissue was carefully peeled off. A 2.5 mm sterilized drill bit was used to drill the skull, and the position was controlled at the left posterior cranial fossa. When there was a sense of breakthrough, the skull piercing was stopped, and dura mater puncturing was avoided. The bone fragments were carefully removed, and the incision was sutured with a thin thread. The incision was disinfected, and the surgery mouse was placed in a new cage. Eight weeks later, the whole skull of the mice was acquired for micro-CT analysis.

Enzyme-linked immunosorbent assay (ELISA)

Serum levels of osteocalcin (*Bglap*) were tested by ELISA according to the manufacturer's instructions (Mouse Osteocalcin ELISA Kit (Colorimetric)). First, 100 μl of Capture Antibody Solution was added into the wells. The plate was incubated

overnight at 4 °C, and the plates were blocked by dispensing 300 µl of reagent diluent into each well and incubating the plate for 60 minutes at room temperature. Then, 100 µl of diluted samples and standards was added to the appropriate wells, and the plate was covered. The plate was incubated for 2 h at room temperature. Finally, 100 µl of Detection Antibody Solution was dispensed into each well. The plate was incubated for 2 h at room temperature. Then, 100 µl of the Substrate Solution was added into each well. The plate was covered and incubated for 20 to 30 minutes at room temperature. After color development, the cover was removed, and 50 µl of Stop Solution was dispensed into each well to stop the enzymatic reaction. The microwell absorbances were read immediately at 450 nm. The mouse serum was collected and diluted 1:20 for measurement of total *Bglap*.

Microcomputed tomography (micro-CT) and histomorphometric analyses

Microcomputed tomography (micro-CT) was used to analyze the bone structure of the femur and skull. The harvested bone tissues were fixed in 4% polyoxymethylene for 2 days and then stored in 70% ethanol at 4 °C before being processed. To analyze trabecular bone, images were acquired at an effective pixel size of 8.82 lm, a voltage of 80 kV, a current of 500 lA and an exposure time of 1500 ms in each of the 360 rotational steps. The bone volume / total volume (BV/TV), bone surface area / bone volume (BSA/BV), trabecular thickness, trabecular number and trabecular spacing were analyzed according to the guidelines. Two-dimensional and three-dimensional bone structure image slices were reconstructed.

H&E, Masson and immunohistochemical staining

The dissected tissues were fixed in 4% polyoxymethylene for 2 days and decalcified in 20% EDTA for 1 week before sectioning. Five-micrometer-thick slices were prepared on charged glass slides. H&E staining and Masson staining were performed according to the manufacturer's instructions (Beijing Solarbio Science & Technology Co., Ltd.). The slides were immersed in 10 mM citrate buffer (pH 7.5) and microwaved at 750 W for 30 minutes for antigen retrieval for immunohistochemical staining. After that, the samples were treated with 3% H_2O_2 for 20 minutes and blocked with 5% normal goat serum for 1 h at room temperature. Primary antibodies were applied in blocking buffer or hybridization buffer at 4 °C overnight. Standard DAB staining was performed for chromogenic detection of immunohistochemistry.

Statistical analysis

Each cellular experimental group was repeated at least three times. All data are expressed as the mean ± standard deviation (SD). Statistical analysis was performed using SPSS 18.0 software (SPSS, Chicago, IL, USA). Statistical significance between *Gas5* heterozygous and wild-type (WT) mice was calculated using a paired two-tailed t test. Statistical differences were analyzed by unpaired two-tailed Student's t test for other comparisons between two groups. Analysis of variance (ANOVA) and appropriate post hoc analyses were used for comparisons of more than two groups. Correlations between the quantification of ARS staining, ALP tests, *ALP*, *RUNX2* and

BGLAP expression and *GAS5* expression in MSCs were examined using Pearson's correlation. A probability value of 0.05 or less was considered statistically significant.

Acknowledgments:

The authors thank American Journal Experts for providing an English language editing service, which was used for this manuscript. **Funding**: This work was supported by grants from the National Natural Science Foundation of China (81971518, 81672097, 81871750, 81702120), the Key Realm R&D Program of Guangdong Province (2019B020236001) and the Fundamental Research Funds for the Central Universities (19ykpy01).

Conflict of interest：The authors declare no conflict of interest.

References:

Anthony BA, Link DC. 2014. Regulation of hematopoietic stem cells by bone marrow stromal cells. *TRENDS IMMUNOL* **35**:32-37. doi:10.1016/j.it.2013.10.002

Berry SD, Shi S, Kiel DP. 2019. Considering the Risks and Benefits of Osteoporosis Treatment in Older Adults. *JAMA INTERN MED* **179**:1103. doi:10.1001/jamainternmed.2019.0688

Bokhari AD, Jonchere V, Lagrange A, Bertrand R, Svrcek M, Marisa L, Buhard O, Greene M, Demidova A, Jia J, Adriaenssens E, Chassat T, Biard DS, Flejou J, Lejeune F, Duval A, Collura A. 2018. Targeting nonsense-mediated mRNA decay in colorectal cancers with microsatellite instability. *ONCOGENESIS* **7**doi:10.1038/s41389-018-0079-x

Cai B, Zhang Y, Zhao Y, Wang J, Li T, Zhang Y, Jiang Y, Jin X, Xue G, Li P, Sun Y, Huang Q, Zhang X, Su W, Yang Y, Sun Y, Shi L, Li X, Lu Y, Yang B, Pan Z. 2019. Long Noncoding RNA–DACH1 (Dachshund Homolog 1) Regulates Cardiac Function by Inhibiting SERCA2a (Sarcoplasmic Reticulum Calcium ATPase 2a). *HYPERTENSION* **74**:833-842. doi:10.1161/HYPERTENSIONAHA.119.12998

Catala M, Khonsari RH, Paternoster G, Arnaud É. 2019. [Development and growth of the vault of the skull]. *Neuro-Chirurgie* **65**:210-215. doi:10.1016/j.neuchi.2019.09.017

Chan WL, Steiner M, Witkos T, Egerer J, Busse B, Mizumoto S, Pestka JM, Zhang H, Hausser I,

Khayal LA, Ott C, Kolanczyk M, Willie B, Schinke T, Paganini C, Rossi A, Sugahara K, Amling M, Knaus P, Chan D, Lowe M, Mundlos S, Kornak U. 2018. Impaired proteoglycan glycosylation, elevated TGF-β signaling, and abnormal osteoblast differentiation as the basis for bone fragility in a mouse model for gerodermia osteodysplastica. *PLOS GENET* **14**:e1007242. doi:10.1371/journal.pgen.1007242

Chen X, Xie R, Gu P, Huang M, Han J, Dong W, Xie W, Wang B, He W, Zhong G, Chen Z, Huang J, Lin T. 2019. Long Noncoding RNALBCS Inhibits Self-Renewal and Chemoresistance of Bladder Cancer Stem Cells through Epigenetic Silencing of SOX2. *CLIN CANCER RES* **25**:1389-1403. doi:10.1158/1078-0432.CCR-18-1656

Compston JE, McClung MR, Leslie WD. 2019. Osteoporosis. *LANCET* **393**:364-376. doi:10.1016/S0140-6736(18)32112-3

de Paula F, Rosen CJ. 2019. Marrow Adipocytes: Origin, Structure, and Function. *ANNU REV PHYSIOL*doi:10.1146/annurev-physiol-021119-034513

de Paula F, Rosen CJ. 2017. Structure and Function of Bone Marrow Adipocytes. *COMPR PHYSIOL* **8**:315-349. doi:10.1002/cphy.c170010

Dehecq M, Decourty L, Namane A, Proux C, Kanaan J, Le Hir H, Jacquier A, Saveanu C. 2018. Nonsense‐mediated mRNA decay involves two distinct Upf1‐bound complexes. *The EMBO Journal* **37**:n/a-n/a. doi:10.15252/embj.201899278

Eastell R, O'Neill TW, Hofbauer LC, Langdahl B, Reid IR, Gold DT, Cummings SR. 2016. Postmenopausal osteoporosis. *NAT REV DIS PRIMERS* **2**doi:10.1038/nrdp.2016.69

Ensrud KE, Crandall CJ. 2017. Osteoporosis. *ANN INTERN MED* **167**:C17-C32. doi:10.7326/AITC201708010

Fiorini F, Robin JP, Kanaan J, Borowiak M, Croquette V, Le Hir H, Jalinot P, Mocquet V. 2018. HTLV-1 Tax plugs and freezes UPF1 helicase leading to nonsense-mediated mRNA decay inhibition. *NAT COMMUN* **9**:431. doi:10.1038/s41467-017-02793-6

Grafe I, Alexander S, Peterson JR, Snider TN, Levi B, Lee B, Mishina Y. 2018. TGF-β Family Signaling in Mesenchymal Differentiation. *CSH PERSPECT BIOL* **10**:a22202. doi:10.1101/cshperspect.a022202

Grayson WL, Bunnell BA, Martin E, Frazier T, Hung BP, Gimble JM. 2015. Stromal cells and stem cells in clinical bone regeneration. *NAT REV ENDOCRINOL* **11**:140-150. doi:10.1038/nrendo.2014.234

Huang Y, Zheng Y, Jia L, Li W. 2015. Long Noncoding RNA H19 Promotes Osteoblast Differentiation Via TGF-beta1/SMAD3/HDAC Signaling Pathway by Deriving miR-675. *STEM CELLS* **33**:3481-3492. doi:10.1002/stem.2225

Infante A, Rodríguez CI. 2018. Osteogenesis and aging: lessons from mesenchymal stem cells. *STEM CELL RES THER* **9**doi:10.1186/s13287-018-0995-x

Katsimbri P. 2017. The biology of normal bone remodelling. *EUR J CANCER CARE* **26**doi:10.1111/ecc.12740

Kim JA, Choi HK, Kim TM, Leem SH, Oh IH. 2015. Regulation of mesenchymal stromal cells through fine tuning of canonical Wnt signaling. *STEM CELL RES* **14**:356-368. doi:10.1016/j.scr.2015.02.007

Li J, Ayoub A, Xiu Y, Yin X, Sanders JO, Mesfin A, Xing L, Yao Z, Boyce BF. 2019. TGF β -induced degradation of TRAF3 in mesenchymal progenitor cells causes age-related osteoporosis. *NAT COMMUN* **10**doi:10.1038/s41467-019-10677-0

Li M, Xie Z, Wang P, Li J, Liu W, Tang SA, Liu Z, Wu X, Wu Y, Shen H. 2018. The long noncoding RNA GAS5 negatively regulates the adipogenic differentiation of MSCs by modulating the miR-18a/CTGF axis as a ceRNA. *CELL DEATH DIS* **9**doi:10.1038/s41419-018-0627-5

Li X, Guo L, Liu Y, Su Y, Xie Y, Du J, Zhou J, Ding G, Wang H, Bai Y, Liu Y. 2017. MicroRNA-21 promotes osteogenesis of bone marrow mesenchymal stem cells via the SMAD7-SMAD1/5/8-RUNX2 pathway. *BIOCHEM BIOPH RES CO* **493**:928-933. doi:10.1016/j.bbrc.2017.09.119

Liu C, Zhang Y, Li R, Zhou L, An T, Zhang R, Zhai M, Huang Y, Yan K, Dong Y, Ponnusamy M, Shan C, Xu S, Wang Q, Zhang Y, Zhang J, Wang K. 2018. LncRNA CAIF inhibits autophagy and attenuates myocardial infarction by blocking p53-mediated myocardin transcription. *NAT COMMUN* **9**doi:10.1038/s41467-017-02280-y

Liu Y, Li G, Zhang J. 2017. The role of long non-coding RNA H19 in musculoskeletal system: A new player in an old game. *EXP CELL RES* **360**:61-65. doi:10.1016/j.yexcr.2017.09.007

Lizneva D, Yuen T, Sun L, Kim S, Atabiekov I, Munshi LB, Epstein S, New M, Zaidi M. 2018. Emerging concepts in the epidemiology, pathophysiology, and clinical care of osteoporosis across the menopausal transition. *MATRIX BIOL* **71-72**:70-81. doi:https://doi.org/10.1016/j.matbio.2018.05.001

Lorentzon M. 2019. Treating osteoporosis to prevent fractures: current concepts and future developments. *J INTERN MED* **285**:381-394. doi:10.1111/joim.12873

M. Plank TD, Wilkinson MF. 2018. RNA Decay Factor UPF1 Promotes Protein Decay: A Hidden Talent. **40**:1700170. doi:10.1002/bies.201700170

Ma Y, Qi M, An Y, Zhang L, Yang R, Doro DH, Liu W, Jin Y. 2018. Autophagy controls mesenchymal stem cell properties and senescence during bone aging. *AGING CELL* **17**:e12709. doi:10.1111/acel.12709

Marchese FP, Raimondi I, Huarte M. 2017. The multidimensional mechanisms of long noncoding RNA function. *GENOME BIOL* **18**:206-213. doi:10.1186/s13059-017-1348-2

Minisola S, Cipriani C, Grotta GD, Colangelo L, Occhiuto M, Biondi P, Sonato C, Vigna E, Cilli M, Pepe J. 2019. Update on the safety and efficacy of teriparatide in the treatment of osteoporosis. *THER ADV MUSCULOSKEL* **11**:1759720X-1987799X. doi:10.1177/1759720X19877994

Miyazawa K, Miyazono K. 2017. Regulation of TGF-β Family Signaling by Inhibitory SMADs. *CSH PERSPECT BIOL* **9**:a22095. doi:10.1101/cshperspect.a022095

Pagnotti GM, Styner M, Uzer G, Patel VS, Wright LE, Ness KK, Guise TA, Rubin J, Rubin CT. 2019. Combating osteoporosis and obesity with exercise: leveraging cell mechanosensitivity. *NAT REV ENDOCRINOL* **15**:339-355. doi:10.1038/s41574-019-0170-1

Ponnusamy M, Liu F, Zhang Y, Li R, Zhai M, Liu F, Zhou L, Liu C, Yan K, Dong Y, Wang M, Qian L, Shan C, Xu S, Wang Q, Zhang Y, Li P, Zhang J, Wang K. 2019. Long Noncoding RNA CPR (Cardiomyocyte Proliferation Regulator) Regulates Cardiomyocyte Proliferation and Cardiac Repair. *CIRCULATION* **139**:2668-2684. doi:10.1161/CIRCULATIONAHA.118.035832

Renganathan A, Kresoja-Rakic J, Echeverry N, Ziltener G, Vrugt B, Opitz I, Stahel RA, Felley-Bosco E. 2014. GAS5 long non-coding RNA in malignant pleural mesothelioma. *MOL CANCER* **13**:119. doi:10.1186/1476-4598-13-119

Roux C, Briot K. 2018. Osteoporosis in 2017: Addressing the crisis in the treatment of osteoporosis. *Nature reviews. Rheumatology* **14**:67. doi:10.1038/nrrheum.2017.218

Sun D, Yu Z, Fang X, Liu M, Pu Y, Shao Q, Wang D, Zhao X, Huang A, Xiang Z, Zhao C, Franklin RJ, Cao L, He C. 2017. LncRNA GAS5 inhibits microglial M2 polarization and exacerbates demyelination. *EMBO REP* **18**:1801-1816. doi:10.15252/embr.201643668

Tang Y, Zhou T, Yu X, Xue Z, Shen N. 2017. The role of long non-coding RNAs in rheumatic diseases. *NAT REV RHEUMATOL* **13**:657-669. doi:10.1038/nrrheum.2017.162

Wang X, Zhao D, Zhu Y, Dong Y, Liu Y. 2019. Long non-coding RNA GAS5 promotes osteogenic differentiation of bone marrow mesenchymal stem cells by regulating the miR-135a-5p/FOXO1 pathway. *MOL CELL ENDOCRINOL* **496**:110534. doi:10.1016/j.mce.2019.110534

Wang Y, Chen W, Lian J, Zhang H, Yu B, Zhang M, Wei F, Wu J, Jiang J, Jia Y, Mo F, Zhang S, Liang X, Mou X, Tang J. 2019. The lncRNA PVT1 regulates nasopharyngeal carcinoma cell proliferation via activating the KAT2A acetyltransferase and stabilizing HIF-1α. *Cell Death & Differentiation*doi:10.1038/s41418-019-0381-y

Wang Y, Shan K, Yao M, Yao J, Wang J, Li X, Liu B, Zhang Y, Ji Y, Jiang Q, Yan B. 2016. Long Noncoding RNA-GAS5 A Novel Regulator of Hypertension-Induced Vascular Remodeling. *HYPERTENSION* **68**:736-748. doi:10.1161/HYPERTENSIONAHA.116.07259

Williams AR, Hare JM. 2011. Mesenchymal stem cells: biology, pathophysiology, translational findings, and therapeutic implications for cardiac disease. *CIRC RES* **109**:923-940. doi:10.1161/CIRCRESAHA.111.243147

Wu M, Chen G, Li YP. 2016. TGF-beta and BMP signaling in osteoblast, skeletal development, and bone formation, homeostasis and disease. *BONE RES* **4**:16009. doi:10.1038/boneres.2016.9

Xie Z, Wang P, Wu Y, Shen H. 2019. Long non-coding RNA: The functional regulator of mesenchymal stem cells. *WORLD J STEM CELLS* **11**:167-179. doi:10.4252/wjsc.v11.i3.167

Xu S, De Veirman K, De Becker A, Vanderkerken K, Van Riet I. 2018. Mesenchymal stem cells in multiple myeloma: a therapeutical tool or target? *LEUKEMIA* **32**:1500-1514. doi:10.1038/s41375-018-0061-9

Yang T, Shen H, Liu A, Dong S, Zhang L, Deng F, Zhao Q, Deng H. 2019. A road map for understanding molecular and genetic determinants of osteoporosis. *NAT REV ENDOCRINOL*doi:10.1038/s41574-019-0282-7

Yao R, Wang Y, Chen L. 2019. Cellular functions of long noncoding RNAs. *NAT CELL BIOL* **21**:542-551. doi:10.1038/s41556-019-0311-8

Yari H, Jin L, Teng L, Wang Y, Wu Y, Liu GZ, Gao W, Liang J, Xi Y, Feng YC, Zhang C, Zhang YY, Tabatabaee H, La T, Yang RH, Wang FH, Yan XG, Farrelly M, Scott R, Liu T, Thorne RF, Guo ST, Zhang XD. 2019. LncRNA REG1CP promotes tumorigenesis through an enhancer complex to recruit FANCJ helicase for REG3A transcription. *NAT COMMUN* **10**doi:10.1038/s41467-019-13313-z

Ye C, Chen M, Chen E, Li W, Wang S, Ding Q, Wang C, Zhou C, Tang L, Hou W, Hang K, He R, Pan Z, Zhang W. 2018. Knockdown of FOXA2 enhances the osteogenic differentiation of bone marrow-derived mesenchymal stem cells partly via activation of the ERK signalling pathway. *CELL DEATH DIS* **9**doi:10.1038/s41419-018-0857-6

Zheng C, Sui B, Qiu X, Hu C, Jin Y. 2020. Mitochondrial Regulation of Stem Cells in Bone Homeostasis. *TRENDS MOL MED* **26**:89-104. doi:10.1016/j.molmed.2019.04.008

Zheng C, Sui B, Qiu X, Hu C, Jin Y. 2019. Mitochondrial Regulation of Stem Cells in Bone Homeostasis. *TRENDS MOL MED*doi:10.1016/j.molmed.2019.04.008

Supplementary files

Supplementary file 1. Primers of the analyzed genes.

Supplementary file 2. The siRNA sequences of the analyzed genes.

Supplementary file 3. Characteristics of the study subjects.

Supplementary file 4. Characteristics of the 15 healthy donors from Center for Biotherapy, Sun Yat-sen Memorial Hospital.

Supplementary file 5. Data of mass spectrometry

Supplementary file 6. Figure Supplement and Figure Supplement legends